

NASA/TP-2003-212156



# Static Aeroelastic Predictions for a Transonic Transport Model Using an Unstructured-Grid Flow Solver Coupled With a Structural Plate Technique

*Dennis O. Allison  
Langley Research Center, Hampton, Virginia*

*Peter A. Cavallo  
The George Washington University  
Joint Institute for Advancement of Flight Sciences  
Langley Research Center, Hampton, Virginia*

---

March 2003

## The NASA STI Program Office . . . in Profile

Since its founding, NASA has been dedicated to the advancement of aeronautics and space science. The NASA Scientific and Technical Information (STI) Program Office plays a key part in helping NASA maintain this important role.

The NASA STI Program Office is operated by Langley Research Center, the lead center for NASA's scientific and technical information. The NASA STI Program Office provides access to the NASA STI Database, the largest collection of aeronautical and space science STI in the world. The Program Office is also NASA's institutional mechanism for disseminating the results of its research and development activities. These results are published by NASA in the NASA STI Report Series, which includes the following report types:

- **TECHNICAL PUBLICATION.** Reports of completed research or a major significant phase of research that present the results of NASA programs and include extensive data or theoretical analysis. Includes compilations of significant scientific and technical data and information deemed to be of continuing reference value. NASA counterpart of peer-reviewed formal professional papers, but having less stringent limitations on manuscript length and extent of graphic presentations.
- **TECHNICAL MEMORANDUM.** Scientific and technical findings that are preliminary or of specialized interest, e.g., quick release reports, working papers, and bibliographies that contain minimal annotation. Does not contain extensive analysis.
- **CONTRACTOR REPORT.** Scientific and technical findings by NASA-sponsored contractors and grantees.
- **CONFERENCE PUBLICATION.** Collected papers from scientific and technical conferences, symposia, seminars, or other meetings sponsored or co-sponsored by NASA.
- **SPECIAL PUBLICATION.** Scientific, technical, or historical information from NASA programs, projects, and missions, often concerned with subjects having substantial public interest.

**TECHNICAL TRANSLATION.** English-language translations of foreign scientific and technical material pertinent to NASA's mission.

Specialized services that complement the STI Program Office's diverse offerings include creating custom thesauri, building customized databases, organizing and publishing research results . . . even providing videos.

For more information about the NASA STI Program Office, see the following:

- Access the NASA STI Program Home Page at <http://www.sti.nasa.gov>
- Email your question via the Internet to [help@sti.nasa.gov](mailto:help@sti.nasa.gov)
- Fax your question to the NASA STI Help Desk at (301) 621-0134
- Telephone the NASA STI Help Desk at (301) 621-0390
- Write to:  
NASA STI Help Desk  
NASA Center for AeroSpace Information  
7121 Standard Drive  
Hanover, MD 21076-1320

NASA/TP-2003-212156



# Static Aeroelastic Predictions for a Transonic Transport Model Using an Unstructured-Grid Flow Solver Coupled With a Structural Plate Technique

*Dennis O. Allison*  
*Langley Research Center, Hampton, Virginia*

*Peter A. Cavallo*  
*The George Washington University*  
*Joint Institute for Advancement of Flight Sciences*  
*Langley Research Center, Hampton, Virginia*

National Aeronautics and  
Space Administration

Langley Research Center  
Hampton, Virginia 23681-2199

---

March 2003

The use of trademarks or names of manufacturers in this report is for accurate reporting and does not constitute an official endorsement, either expressed or implied, of such products or manufacturers by the National Aeronautics and Space Administration.

---

Available from:

NASA Center for AeroSpace Information (CASI)  
7121 Standard Drive  
Hanover, MD 21076-1320  
(301) 621-0390

National Technical Information Service (NTIS)  
5285 Port Royal Road  
Springfield, VA 22161-2171  
(703) 605-6000

**Contents**

List of Tables . . . . . v

List of Figures . . . . . v

Abstract . . . . . 1

Introduction . . . . . 1

Symbols . . . . . 2

Geometry and Cruise Condition . . . . . 3

Computations . . . . . 3

    Fluid Flow . . . . . 4

        Grid Generation . . . . . 4

        Flow Solver . . . . . 4

        Interactive Boundary Layer . . . . . 4

    Structural Deformations . . . . . 5

        Equivalent Plate Representation . . . . . 5

        Rayleigh-Ritz Technique . . . . . 5

        Calibration Procedure . . . . . 6

    Interaction . . . . . 6

Experimental Data . . . . . 7

Results and Discussion . . . . . 8

    Presentation of Results . . . . . 8

    Computed Viscous Effects . . . . . 9

    Computed Elastic Effects . . . . . 9

    Agreement With Experiment . . . . . 10

Concluding Remarks . . . . . 10

Appendix . . . . . 12

References . . . . . 19



**List of Tables**

Table A1. ELAPS Input File . . . . . 16

Table 1. Boundary-Layer Strip Locations . . . . . 20

Table 2. Material Properties for Vascomax T200® . . . . . 20

Table 3. NTF Test 88 Conditions for Cases Calculated. . . . . 20

Table 4. Nominal Location for Lower Surface Orifices. . . . . 20

Table 5. Nominal Location for Upper Surface Orifices. . . . . 21

Table 6. Computed Lift Coefficients, Their Differences, and Comparisons to Experiment . . . . . 21

**List of Figures**

Figure 1. Wing-fuselage configuration of NTF Pathfinder-I lateral controls wing . . . . . 22

Figure 2. Wing planform sketch with pressure orifice rows . . . . . 22

Figure 3. Surface mesh of wing upper surface . . . . . 23

Figure 4. Surface mesh of complete grid . . . . . 23

Figure 5. Plate representation of wing planform . . . . . 24

Figure 6. Procedure for calibration of structural representation. . . . . 25

Figure 7. Static-loading wing-twist increment for calibration of input to ELAPS code . . . . . 25

Figure 8. Flow chart of computational method . . . . . 26

Figure 9. Typical converge history (wind-tunnel case 3,  $M_\infty = 0.819$ ;  $\alpha = 1.98^\circ$ ;  $R_{\bar{c}} = 13.0 \times 10^6$ ;  $q_\infty = 1736$  psf) . . . . . 27

Figure 10. Nominal Reynolds numbers and dynamic pressures . . . . . 27

Figure 11. Wing pressure distributions and deformations for wind-tunnel case 1:  $M_\infty = 0.820$ ;  $\alpha = 1.98^\circ$ ;  $R_{\bar{c}} = 3 \times 10^6$ ;  $q_\infty = 1052$  psf;  $C_L = 0.527$  . . . . . 28

Figure 12. Wing pressure distributions and deformations for wind-tunnel case 2:  $M_\infty = 0.819$ ;  $\alpha = 1.92^\circ$ ;  $R_{\bar{c}} = 13 \times 10^6$ ;  $q_\infty = 1091$  psf;  $C_L = 0.562$  . . . . . 30

Figure 13. Wing pressure distributions and deformations for wind-tunnel case 3:  $M_\infty = 0.819$ ;  $\alpha = 1.98^\circ$ ;  $R_{\bar{c}} = 13 \times 10^6$ ;  $q_\infty = 1736$  psf;  $C_L = 0.541$  . . . . . 32

Figure 14. Wing pressure distributions and deformations for wind-tunnel case 4:  $M_\infty = 0.821$ ;  $\alpha = 1.85^\circ$ ;  $R_{\bar{c}} = 22 \times 10^6$ ;  $q_\infty = 1788$  psf;  $C_L = 0.537$  . . . . . 34

Figure 15. Wing pressure distributions and deformations for wind-tunnel case 5:  $M_\infty = 0.820$ ;  $\alpha = 1.93^\circ$ ;  $R_{\bar{c}} = 22 \times 10^6$ ;  $q_\infty = 2398$  psf;  $C_L = 0.527$  . . . . . 36

Figure 16. Wing pressure distributions and deformations for wind-tunnel case 6:  $M_\infty = 0.820$ ;  $\alpha = 1.88^\circ$ ;  $R_{\bar{c}} = 30 \times 10^6$ ;  $q_\infty = 2429$  psf;  $C_L = 0.514$  . . . . . 38

Figure 17. Effect of Reynolds number on computed viscous decrement in rigid-wing lift coefficient . . . . . 40

Figure 18. Computed wing-twist increment due to aerodynamic load for the six cases . . . . . 40

Figure 19. Effect of dynamic pressure on computed elastic decrement in viscous-flow lift coefficient .....	41
Figure 20. Static-load wing-twist increment for recalibration of input to the ELAPS code .....	41
Figure 21. Effect of more elastic calibration on wing pressure distributions and deformations for wind-tunnel case 3: $M_\infty = 0.819$ ; $\alpha = 1.98^\circ$ ; $R_c = 13 \times 10^6$ ; $q_\infty = 1736$ psf; $C_L = 0.541$ .....	42



## Abstract

*An equivalent-plate structural deformation technique was coupled with a steady-state unstructured-grid three-dimensional Euler flow solver and a two-dimensional strip interactive boundary-layer technique. The research objective was to assess the extent to which a simple accounting for static model deformations could improve correlations with measured wing pressure distributions and lift coefficients at transonic speeds. The structural technique used a Rayleigh-Ritz solution and modeled the wing planform as well as the wing thickness and camber distributions. Computational efficiency came from two sources: the use of a structural plate technique rather than a finite-element method and the use of an Euler solver with interactive boundary layer rather than a Navier-Stokes solver. Results were computed for a wing-fuselage model of a generic low-wing transonic transport and were compared to test data from the National Transonic Facility at Langley Research Center. Comparisons were made at a transonic cruise condition over a range of Reynolds numbers and dynamic pressures. Nominally, the Mach number was 0.82, the lift coefficient was 0.55, the Reynolds number range was  $3 \times 10^6$  to  $30 \times 10^6$ , and the dynamic pressure range was 1100 to 2400 psf. The deformations significantly improved correlations with measured wing pressure distributions and lift coefficients. This method provided a means of quantifying the role of dynamic pressure in wind-tunnel studies of Reynolds number effects for transonic transport models.*

## Introduction

An aircraft wing in flight or a subscale model wing in a wind tunnel will deform under aerodynamic load. All wings experience aeroelastic deformation to varying extents, but transonic transport wings, because of their high aspect ratios, are particularly susceptible to significant deformations. Also, even if a wing is designed to deform to a given shape at a given flow condition, it will take on different shapes at other conditions. The pressure distributions (hence loading) on an aeroelastically deformed wing may be significantly different from those on a rigid wing. A typical transonic transport wing is swept back and the tip twists down when aerodynamic lift deflects the wing upward, resulting in decreased incidence (and lift) toward the wing tip (ref. 1). In transonic flows, this unloading of the wing causes the shock to move forward toward the tip and significantly alters wing performance. Therefore, the accuracy of predicted wing pressure distributions may be greatly improved by accounting for static aeroelastic effects.

Studies of Reynolds number effects for a transonic transport model in a wind tunnel can be complicated by the effects of free-stream dynamic pressure, since

dynamic pressure is generally increased to achieve high Reynolds numbers. When Reynolds number and dynamic pressure are both increased, they have opposite effects on pressure distributions and lift coefficients. As Reynolds number is increased, lift coefficient is increased because the boundary layer is thinner and has less decambering effect on the supercritical wing. As dynamic pressure is increased, lift coefficient is decreased because the higher loading causes more deformation, resulting in decreased incidence toward the wing tip. The effects of each of these two variables can be computed separately.

The computation of static aeroelastic flow characteristics involves the interaction between aerodynamic loads and structural deformations under steady-state flow conditions. Dynamic aeroelasticity involves unsteady flows interacting with transient structural deformations. Only static aeroelasticity was considered herein. Since an aeroelastically deformed wing can produce a significantly different pressure distribution than a rigid wing, the elastic deformation can be instrumental in determining the aerodynamic loading (ref. 2). The interaction between the load distribution resulting from a specified wing shape and the wing shape resulting from a specified load distribution may be treated numerically as an iterative process which is

followed until the structural shape is consistent with the load distribution.

Detailed analyses of wing deformations can be performed with finite-element techniques. However, development of finite-element representations requires a substantial amount of effort, and large computer resources (both memory and solution time) are required to obtain solutions. The complexity deters routine calculation, and the solution time is an issue in iterative situations. Equivalent plate structural analysis techniques have shown accuracies adequate for preliminary analysis and design purposes while requiring substantially smaller computer resources (ref. 3). Thus, such techniques are good candidates for coupling with computational fluid dynamics (CFD) codes for efficient static aeroelastic analysis. The simplification of the approximate techniques follows from assuming that the deformations can be represented in a functional form. The Equivalent Laminated Plate Solution (ELAPS) structural code employed a Rayleigh-Ritz technique to compute wing deformations in the form of a polynomial (refs. 3 and 4). In contrast to finite-element models, the degrees of freedom were not the displacements but the coefficients of an assumed displacement polynomial. As a result, a much smaller matrix equation was solved than with a finite-element representation, greatly decreasing computation time.

The equivalent plate technique was coupled with a steady-state unstructured-grid Euler solver and a two-dimensional strip interactive boundary layer (IBL) to create an efficient combined fluid-dynamic/structural analysis method (ref. 5). Unstructured grids are readily generated around complex aircraft geometries. The Euler/IBL approach is valid for transonic transport configurations under a variety of conditions up to mild separation (ref. 6). With each structural computation, the CFD grid must be altered to conform to the new deformed surface shape. The displacement polynomial of the equivalent plate technique allows deformations to be evaluated at any location, which is ideal for interaction with an unstructured grid.

This computational aeroelastic method was applied to a subscale wind-tunnel model consisting of only a wing and a fuselage at cruise Mach number and lift conditions. This wing and fuselage modeled a generic transonic transport configuration. The model

wing included internal cavities, cover plates, and removable inboard and outboard ailerons. However, for simplicity, the wing was represented in this paper as a solid structure which was inherently too stiff. A simple calibration procedure was used to make the representation more flexible; the stiffness of the wing was reduced until deformations computed for a given point load agreed with deformations measured under the same point load. The objective of this research was to assess the extent to which this simple accounting for static model deformations could improve correlations with measured wing pressure distributions and lift coefficients at transonic speeds. The predictive capability of the aeroelastic method was demonstrated for wide ranges of Reynolds number and dynamic pressure by comparing computed wing pressure distributions and lift coefficients with experimental data. Also, the differences between wing pressure distributions and lift coefficients computed with and without the structural deformations revealed a significant influence of dynamic pressure in the experimental data.

## Symbols

$A_z$	projection of wing grid-cell face area in plane normal to $z$ axis
$b$	model span, 52.96 in.
$C_L$	lift coefficient, $\frac{\text{Lift}}{q_\infty S_{\text{ref}}}$
$C_p$	pressure coefficient, $\frac{p - p_\infty}{q_\infty}$
$c$	wing local chord, in.
$\bar{c}$	wing mean aerodynamic chord, 5.74 in.
$F_z$	$z$ -component of force on wing grid-cell face center, lb
$f_0$	single calibration factor
$f_1$	plate 1 calibration factor
$f_2$	plate 2 calibration factor
$M_\infty$	free-stream Mach number

$p$	local static pressure, psf
$p_\infty$	free-stream static pressure, psf
$q_\infty$	free-stream dynamic pressure, psf
$R_{\bar{c}}$	Reynolds number based on wing mean aerodynamic chord
$S_{\text{ref}}$	wing reference area (trapezoidal extended to centerline), 286.34 in <sup>2</sup>
$x$	longitudinal coordinate in body axis system, in.
$y$	lateral coordinate in body axis system, in.
$z$	normal coordinate in body axis system, in.
$\alpha$	model angle of attack, deg
$\eta$	wing semispan fraction, $2y/b$

#### Abbreviations:

CFD	computational fluid dynamics
CPU	central processing unit
ELAPS	Equivalent LAMinated Plate Solution structural code
IBL	interactive boundary layer
NTF	National Transonic Facility
Res	USM3D code convergence residual
USM3D	UnStructured Mesh 3-Dimensional flow solver code
VGRID	unstructured grid generator code

## Geometry and Cruise Condition

The computational method was applied to a National Transonic Facility (NTF) wing-fuselage model of a generic low-wing transonic transport. The wing-fuselage configuration for which solutions were

calculated had no control surface deflections, no engine nacelle, and no tail. The model was known as the NTF Pathfinder-I lateral controls wing (fig. 1, spoiler control surface was deflected in photograph). It had the fuselage and the wing planform and dihedral of that reported in reference 7 as well as similar supercritical airfoil sections with blunt trailing edges. The configuration also had wing-fuselage fillets and a 10.5-in. fuselage extension ahead of the wing that were not present in reference 7.

The wing had a planform break at  $\eta = 0.376$ , with extended chord lengths inboard of this location (fig. 2). Wing attributes based on the trapezoidal reference planform (omitting leading and trailing edge extensions inboard of the planform break) included an area of 286.34 in<sup>2</sup>, a span of 52.96 in., a mean aerodynamic chord of 5.74 in., an aspect ratio of 9.8, a taper ratio of 0.40, a quarter-chord sweep of 30°, and a dihedral of 5°. The wing and a portion of the fuselage were a single structure mounted in a cutout in the bottom of the fuselage. The length of the fuselage was 60.5 in. and it was defined by circular cross sections with a 5.75 in. diameter in the vicinity of the wing.

The design cruise condition was a lift coefficient of 0.55 at a free-stream Mach number of 0.82. Calculations were performed at wind-tunnel conditions that approximated this condition for a variety of Reynolds numbers and dynamic pressures. A design cruise Reynolds number was not defined, as the wind-tunnel model was not a representation of a full-scale aircraft. Because a design Reynolds number (and therefore tunnel dynamic pressure) was not defined, the model wing was not designed to aeroelastically deform to a cruise shape. Wing deformations were calculated relative to the unloaded shape, not to a cruise shape.

## Computations

This section describes the fluid flow and structural deformation solution techniques and their interaction. Because of the iterative nature of computations, a typical solution process consisted of several steps. The Euler flow, boundary-layer transpiration velocity and structural-deformation calculations interacted with each other in an iterative procedure until convergence was achieved (ref. 5).

## Fluid Flow

A steady-state unstructured-grid Euler flow solver, coupled with an interacting boundary layer (refs. 6 and 8), was used to obtain flow solutions in the present work. The wing boundary layer was computed by using a two-dimensional strip method. The fuselage boundary layer was neglected as it was not expected to have much influence on wing pressure distributions. This Euler flow, interacting-boundary-layer approach allowed wing pressure distributions to be efficiently obtained.

## Grid Generation

The unstructured grid generator VGRID (ref. 9) was used to create discretized surface and volume meshes by the advancing front method (ref. 10). To create the surface mesh, the surface definition was first subdivided into a series of three- or four-sided patches. Next, a surface mesh was generated on the interior of each patch and projected onto the surface geometry definition to ensure surface mesh fidelity (ref. 11). The volume grid was generated by VGRID and improved through use of a postprocessing technique in which poor quality cells were removed and more uniform cells were locally created (ref. 9). Side-slip was not considered in the cases simulated herein; thus, only half the configuration was modeled and symmetry conditions were applied on the centerplane. Grid cells were generally clustered near the surface where large flow gradients were expected to exist. On the wing, points were clustered at the leading and trailing edges, the tip, and on the upper surface where a shock was anticipated. Points were also clustered at the nose of the fuselage.

The grid was generated for a free-air simulation of flow about the configuration described earlier, consisting of a wing and a fuselage with fillets between them. Figures 3 and 4 depict the wing-fuselage surface grid. Surfaces with grid included the blunt trailing edge of the wing and the base of the fuselage. The sting that held the model in the wind tunnel was not represented. The grid had 10 882 surface points, 85 909 points, and 471 173 cells. The upstream and downstream boundaries were located approximately 3.5 fuselage lengths from the fuselage (or approximately 37 mean-aerodynamic-chord lengths). The top, bottom, and spanwise boundaries were located

approximately 2.5 semispan lengths from the wing (12 mean-aerodynamic-chord lengths). Although no grid-convergence assessment was made as part of this study, the grid used was consistent with sensitivity studies by Cavallo and Smith (refs. 5 and 6).

## Flow Solver

The USM3D flow solver code (version USM44n, refs. 12 and 13) used to obtain all solutions is a code that solves the three-dimensional Euler equations on unstructured tetrahedral grids for cell-centered flow quantities. Roe's upwind flux difference splitting was used for inviscid flux computations across cell faces (ref. 14), and boundary conditions were applied at cell face centers. The code required 180 words/cell of central computer memory and 347  $\mu\text{s}$ /cell/iteration of single-processor central processing unit (CPU) time on a Sun® Ultra 2 ULTRASPARC workstation. Solutions were judged to have converged when the lift coefficient had converged to three decimal places. In conjunction with this criterion, the residual typically dropped by approximately three orders of magnitude.

Characteristic boundary conditions were applied on all far-field boundaries. A flow tangency boundary condition was used on inviscid surfaces and on the centerline symmetry plane. For viscous surfaces, the flow tangency condition was modified to allow a non-zero velocity through a surface. The normal component of velocity was the transpiration velocity which compensated for the displacement thickness (ref. 6). The wing blunt trailing edge and the fuselage base were treated with a solution-dependent transpiration boundary condition which simulates the presence of a wake. This condition averages the primitive flow variables from appropriate grid-cell corners to each surface grid-cell face; it is a refinement of a condition developed in reference 15. As a result, the flow departs smoothly rather than trying to turn across a sharp corner.

## Interactive Boundary Layer

As noted previously, an approximate boundary layer was computed for the wing but not for the fuselage. The boundary-layer technique is detailed in reference 6 and summarized here. It was a steady, incompressible, two-dimensional strip method with an

algebraic eddy-viscosity turbulence model (ref. 16) and has shown good agreement with experiment for transonic flow up to and including mild separation (ref. 17). It was an inverse method whereby the boundary-layer edge velocity was found iteratively, and Keller's box method (ref. 18) was used to solve the finite difference form of the equations. Separated regions were approximated by setting the convective term to zero in recirculating regions. A laminar boundary layer was computed upstream of the boundary-layer transition location. The boundary layer was assumed to be fully turbulent for calculations at chord Reynolds numbers above  $20 \times 10^6$ . For solutions at  $R_c = 3 \times 10^6$  and  $13 \times 10^6$ , the wing upper and lower surface transition location was specified to correspond to experiment.

Boundary-layer calculations were performed at a series of chordwise strips to yield displacement thickness values. The displacement thicknesses along each strip were converted to transpiration velocities. Interpolation was used to determine values of transpiration velocity at all wing surface nodes between boundary-layer strips (ref. 6). Table 1 lists the eight spanwise locations of the boundary-layer strips used in this work; the first and last strip locations corresponded to the approximate wing root and tip locations, and the transpiration velocity was assumed to be zero inboard of the first and outboard of the last strip.

## Structural Deformations

Static aeroelastic deformations were calculated relative to the unloaded wing shape by using an equivalent plate method, Equivalent Laminated Plate Solution (ELAPS) (refs. 3 and 4). The ELAPS method was capable of computing wing structural deformation due to applied forces, aerodynamic loads, and thermal loads; only applied forces and aerodynamic loads were considered. Both static and dynamic analyses could be performed; only static analyses were considered. An equivalent plate method was applicable because the wing stiffness could be represented as a continuous distribution over each of a series of plates. A Rayleigh-Ritz technique (ref. 19) was used to perform structural analyses and provided estimates of wing deformations. A simple calibration procedure was used to compensate for approximations in the representation of the geometry and in the structural analysis.

The equivalent plate representation, the Rayleigh-Ritz technique, and the calibration procedure are discussed next. The preparation of the ELAPS input file for the calibrated structural representation is discussed in the appendix.

### *Equivalent Plate Representation*

The wing geometry was represented by two trapezoidal plates, as shown in figure 5. The origin of the body ( $x,y,z$ ) axis system was located 10.5 in. behind the nose on the fuselage centerline. The wing root (chosen as  $y = 3.26$  in.,  $\eta = 0.123$ ) was close to but outboard of the wing-fuselage junction. The wing was cantilevered from this station. Each plate was defined by a planform, thickness distribution, camber distribution, and material properties. Thickness and camber distributions were defined from the original wing surface definition in the chordwise direction at the inboard and outboard edges of each plate. A linear variation in the spanwise direction was specified to form a complete distribution of both thickness and camber. Wing plates could either be solid, as in the present application, or composed of skin layers and other components. The material properties for the steel from which the model was fabricated are listed in table 2. The properties that were specified for the wing plates were calibrated as explained below under "Calibration Procedure."

### *Rayleigh-Ritz Technique*

Rayleigh-Ritz techniques are approximate solutions in which it is assumed that displacements can be described by functions such as polynomials. The present Rayleigh-Ritz technique determined an approximate stationary value for the total potential energy of the structure (ref. 5). When the total potential energy of a deformed structure was minimized, the structure was in equilibrium. The method was applied to an assumed displacement polynomial by requiring that the total potential energy be stationary with respect to each polynomial coefficient. This application of the Rayleigh-Ritz technique led to a set of linear simultaneous equations for the unknown coefficients.

The Rayleigh-Ritz technique employed in ELAPS obtained the structural solution for a specified wing load distribution. Global displacement polynomials

were produced which automatically satisfied continuity across plates. The polynomial terms were specified by the user and the unknown coefficients were determined. Certain terms in these polynomials were omitted to constrain the displacement and its slope to zero at the inboard edge of plate 1. Typical upper limits on these polynomials are fifth order in  $x$  and eighth order in  $y$  for static analyses (ref. 3). This limitation was imposed by the ill-conditioned matrix equation which could result with higher order polynomials (ref. 4). The current application used terms up to third order in  $x$  and fifth order in  $y$ . Displacements of a planar ( $x$ - $y$ ) reference surface in the  $x$ ,  $y$ , and  $z$  directions were computed. Deformations of the wing were then computed from only the  $z$ -direction displacement polynomial in the present work. It was shown in reference 5 that displacements in the  $x$  and  $y$  directions had negligible effects on the wing pressure distributions.

### **Calibration Procedure**

Structural model approximations occurred in both the equivalent plate representation of the wing geometry and in the Rayleigh-Ritz functional description of the wing deformations. The effect of both was to cause the solution to be too stiff. For example, the structural model of the wing was solid, while the wind-tunnel model had internal cavities, cover plates, and removable ailerons. To a lesser extent, the functional description of the deformations constrained the structural model from deforming exactly as the wind-tunnel model would.

A simple calibration procedure was used in the present work to compensate for the above approximations. The calibration procedure was based on a match between measured and computed twist increment due to a point load (fig. 6). The wind-tunnel model was mounted in an inverted orientation, and a weight hanger was used to apply a load to an outboard point on the wing (currently at 0.89 semispan and 53 percent local chord). Leading and trailing edge positions were measured in the vertical direction at given spanwise locations with and without the load. These vertical positions were used to determine a measured spanwise twist increment caused by the load. The ELAPS code was run with and without the same load and a computed spanwise twist increment due to the load was determined. These computed increments in twist angle were, as expected, smaller than the measured ones.

Next, Young's modulus and shear modulus were multiplied by a calibration factor,  $f_0$ , of less than one to make the structural model more flexible. The ELAPS code was run, and the factor was adjusted until the computed increments in twist angle agreed approximately with the measured ones ( $f_0 = 0.3250$ ). The spanwise agreement was improved in the present work (fig. 7) by using separate calibration factors on the separate structural plates ( $f_1 = 0.1165$  and  $f_2 = 0.4660$ ). Thus, the present structural representation had two plates with different calibration factors. The calibration factors will vary from problem to problem, either for a new structural representation of the same aircraft model (e.g., more detailed), or for a different aircraft model. The preparation of the ELAPS input file for the present calibrated structural representation is discussed in the appendix. The input file was prepared for the March 1998 version of the ELAPS code.

### **Interaction**

Several steps were performed to couple the flow solution with the structural method and obtain an elastic solution whose wing shape was consistent with the aerodynamic loads. This process (fig. 8) was automated in a modular fashion (ref. 20) by using pre- and postprocessors so that the flow solver, the boundary-layer solver, or the structural solver could be replaced individually. An initial inviscid solution (which need only be partially converged, 50 iterations herein) was obtained to generate an estimate of the flow over the geometry being modeled. The boundary-layer and structural methods were then simultaneously applied at constant intervals through the remaining iterations. The update frequency was once every 10 USM3D iterations for calculations presented herein. The boundary layer did not impact the grid because it interacted by way of transpiration velocities. The aerodynamic loads were applied on the wing as concentrated forces acting at grid-cell face centers. Pressure coefficients  $C_p$  were obtained from the flow solver for all cell faces on the wing. Each coefficient was converted into a concentrated force in the body coordinate  $z$  direction as  $F_z = C_p A_z q_\infty$  where  $A_z$  was the projection of the face area and  $q_\infty$  was the free-stream dynamic pressure. These forces were passed to the ELAPS structural module and the displacements were computed. The continuous polynomial definition allowed displacements to be evaluated at any location, which

was convenient for interaction with the unstructured mesh. The surface mesh was deformed only in the  $z$  direction. Displacements were applied at nodes and were always added to the original surface because the plate representation approximated the original wing. The first time surface displacements were computed they were multiplied by 0.5 to avoid overshoot because the first flow solution (inviscid) was expected to result in too much load. This technique produced a more favorable convergence behavior and improved the robustness of the spring analogy discussed next.

The interaction featured an existing method to displace points in the grid. Once the surface mesh was moved, the nodes in the volume grid were moved by using a spring analogy to assimilate the surface geometry changes due to aeroelastic deformation into the surrounding grid (ref. 21). Each edge of a tetrahedron was modeled as a spring whose stiffness was inversely proportional to the distance between the two nodes. At the far field, the nodes were fixed. The equations of equilibrium were then employed to compute the node displacements by using a predictor-corrector scheme. The deformed grid was used without further modification because the grid connectivity and boundary conditions remained unchanged. After the points in the mesh were displaced, the flow solution was restarted with the updated grid and the updated transpiration velocities.

A process referred to as a cycle was repeated in regular intervals until the structural deformations, boundary layer, and aerodynamic loads converged. A cycle consisted of 10 USM3D iterations and an update of both the boundary layer and the deformations. A typical convergence history (for case 3 of table 3) is given in figure 9. Note that the small disturbances in the residual tended to disappear as additional cycles were performed. The convergence criterion was that the lift coefficient converge to three decimal places between cycles. Cavallo (ref. 5) used 50 USM3D iterations per cycle and converged the viscous solution before starting the elastic solution; this resulted in a total of 650 iterations for a typical convergence history. He suggested starting the deformations earlier and updating them more often as in the present work where the typical convergence history required only 250 iterations. Because the USM3D flow solver required 347  $\mu$ s/cell/iteration of single-processor CPU time on a Sun® Ultra 2 ULTRAPARC workstation and there were 471 173 cells in the grid, 250 iterations

required about 11 hours. Additional computer time, probably about 1 hour, was required for the boundary layer, structural deformation, and grid movement activities.

## Experimental Data

Aerodynamic force and wing pressure measurements for the low-wing transonic transport model described earlier were available from test 88, performed in the National Transonic Facility (NTF) at NASA Langley Research Center. Some information about the test is available in reference 22 where it is referred to as the outboard aileron test. The experimental data allowed the evaluation of the computational method across a chord Reynolds number range of  $3 \times 10^6$  to  $30 \times 10^6$  and over a factor of 2.3 change in free-stream dynamic pressure. Six cases were chosen to cover these ranges; table 3 lists the corresponding test conditions, test gases, run numbers, and point numbers. The following paragraphs discuss the NTF, boundary-layer transition, force and moment data, and wing pressure data.

Since the experimental data used herein are unpublished, some facility details are presented. The NTF (refs. 23 and 24) is a pressurized, continuous-flow, transonic wind tunnel capable of testing at unit Reynolds numbers of  $4 \times 10^6/\text{ft}$  to  $145 \times 10^6/\text{ft}$ . The Mach number range is from subsonic (0.1) to low supersonic (1.2), with a pressure range from 1 to approximately 9 atm. The temperature is variable from  $-250$  to  $+150$  °F with a test gas of nitrogen at all temperatures or dry air at high temperatures. The test section has a cross section of 8.2 by 8.2 ft and a length of 25 ft. Longitudinal slots in the floor and ceiling provide a 6-percent wall-openness ratio.

Boundary-layer transition was artificially fixed on the wing upper and lower surfaces at a forward location to maintain a stationary transition at chord Reynolds numbers of  $3 \times 10^6$  and  $13 \times 10^6$ . The fixed transition location varied linearly from 5 percent local chord at the wing root to 10 percent local chord at the tip. Transition was performed by using disk-type trips (ref. 25) with a height of 0.0037 in., a diameter of 0.045 in., and center spacing of 0.100 in. Natural transition was allowed at  $R_c > 20 \times 10^6$  because it was estimated to occur within the first 5 percent of local chord.

Force and moment data were measured by using a 6-component strain-gage balance designated NTF-113 B in test 88. This balance was designed for the following maximum loads: normal force, 6500 lb; axial force, 400 lb; pitching moment, 13 000 in-lb; rolling moment, 9000 in-lb; yawing moment, 6500 in-lb; and side force, 4000 lb. The balance had a quoted accuracy of at least  $\pm 0.5$  percent of design full-scale load. Model angle of attack was measured with an internal, heated, single-axis accelerometer with a quoted accuracy of  $\pm 0.01^\circ$  for small angles. Standard balance, angle-of-attack, and tunnel-parameter corrections were made. Balance output was compensated for differences in balance temperature between the wind-on and wind-off conditions. There were three balance thermocouples, and the output of each gage was corrected by using readings from the closest thermocouple. Axial force data were corrected for the difference between measured balance chamber pressure and free-stream static pressure. An angle-of-attack correction for upflow in the test section was determined from data acquired by running at the same tunnel conditions with the model upright and inverted. The upflow angles were from  $0.10^\circ$  to  $0.15^\circ$  for the current test conditions. The test section was slotted and wall interference corrections were not made for the present data. The uncertainty in  $C_L$  was estimated in reference 22 from the accuracy of the measurement instruments using the technique described in reference 26. The uncertainties in  $C_L$  were 0.0025, 0.0016, and 0.0011 (ref. 22, outboard aileron test) for nominal dynamic pressures of 1100, 1800, and 2400 psf, respectively. Repeat runs were obtained at a Mach number of 0.82 and a Reynolds number of  $3 \times 10^6$ . These runs were analyzed in reference 22 to assess the data repeatability using the regression statistical analysis of reference 27. In reference 22 it was stated that, in general, the repeatability was good, with the confidence interval similar in magnitude to the measurement uncertainty.

The seven rows of pressure orifices used for obtaining wing pressure data are given in figure 2. Nominal chordwise locations of orifices at each span station are given for the lower and upper surfaces in tables 4 and 5. The large number (258) of wing pressure orifices were distributed over both wings to accommodate the volume of the pressure tubing. Lower surface orifices were distributed over the right-hand wing and upper surface orifices over the left-

hand wing. Six heated, 48-port, electronically scanned pressure modules were used to measure wing pressures. The modules were matched with expected local wing pressure ranges. The three lower surface modules had a full-scale differential pressure range of  $\pm 30$  psi, and the three upper surface modules had a range of  $\pm 45$  psi. Their quoted accuracy throughout each range was  $\pm 0.20$  percent of full scale.

## Results and Discussion

Computations were performed at the Mach-number, angle-of-attack, Reynolds-number, and dynamic-pressure conditions in table 3 from NTF test 88. All six of these cases were chosen to be close to the cruise Mach number and lift condition ( $M_\infty = 0.82$ ,  $C_L = 0.55$ ) while including chord Reynolds numbers of  $3 \times 10^6$ ,  $13 \times 10^6$ ,  $22 \times 10^6$ , and  $30 \times 10^6$  and a wide range of dynamic pressures. The progression from case 1 to case 6 involved alternately increasing Reynolds number while holding dynamic pressure constant and increasing dynamic pressure while holding Reynolds number constant. Figure 10 depicts the resulting stair-step array of dynamic pressures (nominally 1100, 1800, and 2400 psf) at the given Reynolds numbers. Note that the stair-step array has three horizontal (constant dynamic pressure) segments and two vertical (constant Reynolds number) segments. After results are presented, discussions will be given concerning computed viscous effects along the horizontal segments, computed elastic effects along the vertical segments, and agreement with experimental data.

## Presentation of Results

Results are given in figures 11–16 for the six cases considered. Each figure displays experimental and computational lift coefficients and wing pressure distributions as well as computational deflections ( $z$  versus  $x/c$ ). Symbols represent NTF wind-tunnel data and lines represent computational results. The rigid-inviscid and rigid-viscous results were both for the rigid shape but without and with the boundary layer, respectively. The elastic-viscous results included the effects of both the boundary layer and the structural deformations. Computed lift coefficients, their differences, and comparisons to experiment are summarized in table 6. Computed viscous lift-coefficient decrements from table 6 are plotted in figure 17.



Computed wing-twist increments due to aerodynamic load are plotted in figure 18 for the six cases. Computed elastic lift-coefficient decrements from table 6 are plotted in figure 19. Figures 20 and 21 (which are similar to figs. 7 and 13) relate to recalibrating the inputs to the ELAPS code. The next three sections discuss computed viscous effects (difference between rigid-inviscid and rigid-viscous results), computed elastic effects (difference between rigid-viscous and elastic-viscous results), and agreement with experiment (difference between elastic-viscous results and NTF data).

### Computed Viscous Effects

The interactive boundary layer was the computational means for estimating viscous effects. The boundary layer had a large influence on computed pressure distributions and lift coefficients (figs. 11–16 and table 6), primarily by effectively decambering the rear part of the wing, which occurred through the wing upper surface boundary-layer thickening toward the trailing edge and the lower surface boundary-layer filling in the concave region ahead of the trailing edge. Two effects on wing pressure distributions were observed for all six cases (difference between rigid-inviscid and rigid-viscous): (1) the shock moved forward toward the experimental location (forward by about 15 to 25 percent of chord) at all wing span stations, and (2) the upper and lower surface pressure levels moved toward each other (as well as toward the experimental data) especially at the outer span stations. These effects occurred simultaneously and both caused a decrease in the lift coefficient. For simplicity, the discussion that follows is limited to lift coefficient decrease as it represents both effects.

Viscous lift-coefficient decrements are greatest at the lowest Reynolds number but are still important at the highest Reynolds number (see table 6). The greatest difference between rigid-inviscid and rigid-viscous results occurred for case 1 in figure 11, where the lowest Reynolds number ( $R_c = 3 \times 10^6$ ) resulted in the thickest boundary layer; the lift coefficient decreased by 0.234. By contrast, the smallest difference between rigid-inviscid and rigid-viscous results occurred for case 6 in figure 16 ( $R_c = 30 \times 10^6$ ); the lift coefficient decreased by 0.152. Viscous lift-coefficient decrements from table 6 are plotted in figure 17 to further

illustrate that, as  $R_c$  increases, there is less lift loss as the decambering effect of the boundary layer weakens.

### Computed Elastic Effects

Even though the wind-tunnel model was less flexible than a full-scale flight vehicle, the model wing did bend and twist under load. As described earlier, the transport model wing had an aspect ratio of 9.8 and a quarter chord sweep of  $30^\circ$ . The sweep resulted in a nose-down twisting due to spanwise bending under aerodynamic load and a corresponding lowering of local lift toward the wing tip. The interactive structural deformation technique was the computational means for estimating elastic effects. The six curves of computed wing-twist increment due to aerodynamic loads in figure 18 group themselves into three pairs for the three nominal dynamic pressures. The magnitude of the twisting increases as dynamic pressure (hence wing load) increases between pairs of curves.

The structural deformations had an important influence on computed pressure distributions and lift coefficients (figs. 11–16 and table 6). As with viscous effects, two effects of elasticity on the wing pressure distributions were observed for all six cases (difference between rigid-viscous and elastic-viscous): (1) the shock moved forward and was closer to the experimental location at all wing span stations, and (2) the upper and lower surface pressures moved closer to each other and more closely matched the experimental data, especially at the outer span stations. These effects occurred simultaneously and both caused a decrease in lift coefficient relative to the rigid results. Again for simplicity, the discussion that follows is limited to lift-coefficient decrease as it represents both effects.

The elastic effects were in all cases (figs. 11–16) significant, especially at the outboard stations where the deformations  $z$  due to wing load and the corresponding twist increments were greater than at the inboard stations (fig. 18). Note that the elastic-viscous results were in much better agreement with the NTF data than the rigid-viscous results (see table 6). The difference between rigid-viscous and elastic-viscous results was moderate for case 1 in figure 11 because the low dynamic pressure ( $q_\infty = 1052$  psf) resulted in moderate deformations; the lift coefficient decreased by 0.050. By contrast, larger differences occurred for

case 6 in figure 16 because the higher dynamic pressure ( $q_\infty = 2429$  psf) resulted in larger deformations; the lift coefficient decreased by 0.127. Elastic lift decrements from table 6 are plotted in figure 19 to further illustrate that, as  $q_\infty$  increases, there is more lift loss due to aeroelastic-induced twist effects.

The computational results revealed the separate effect of either Reynolds number or dynamic pressure on the lift coefficient for each segment of the array in figure 10. On the horizontal segments, the lift-coefficient decrements decreased (fig. 17), while on the vertical segments they increased (fig. 19). Thus, dynamic pressure had the opposite effect as Reynolds number, which could complicate wind-tunnel studies of Reynolds number effects when both are varied simultaneously. The magnitude of the elastic effects provided a measure of the influence of dynamic pressure.

### Agreement With Experiment

The computed elastic-viscous wing pressure distributions for all cases (figs. 11 to 16) agreed well with the NTF data. The shock locations at the various wing span stations were correctly predicted or only slightly downstream of the NTF data. The upper and lower surface pressure levels were only slightly underpredicted and overpredicted, respectively. The total lift coefficient was overpredicted by 0.050 to 0.059 (see difference from experiment in table 6 which is the difference between elastic-viscous  $C_L$  and NTF  $C_L$ ). However, the overprediction does not display much dependence on Reynolds number or dynamic pressure; its variation is small compared to the variation in computed viscous or elastic lift-coefficient decrements, which means that trends in the viscous and elastic decrements in lift coefficient should not be affected by the overpredicted lift coefficient.

The overpredicted lift coefficient was partially reflected in the small discrepancies in shock location and upper and lower surface pressure levels at the various span stations. Because it was more evident outboard than inboard, it could have been caused at least in part by too much stiffness in the structural representation. To make a rough check, the representation was made more elastic by lowering the two calibration factors to  $f_1 = 0.100$  and  $f_2 = 0.400$ . The more elastic

calibration is shown in figure 20, along with the two-factor calibration from figure 7. The more elastic calibration was better in the region around  $\eta = 0.5$  to 0.6, and it overshoot the data outboard. The agreement with experimental data was improved for case 3 (fig. 21), but only enough to further decrease the lift coefficient by 0.012. It appeared that if improvements in the structural representation and calibration (such as more plates and calibration factors) could help, they would account for less than half the overprediction of the lift coefficient. Because the overprediction was relatively constant for the range of conditions studied, it could be associated with factors not assessed in this study that are somewhat insensitive to Reynolds number and dynamic pressure. Examples could include fuselage loads, higher order flow modeling effects, or numerical uncertainty. Experimental uncertainty could also be a factor.

### Concluding Remarks

A structural plate technique coupled with an unstructured-grid Euler flow solver and a two-dimensional strip boundary-layer technique determined static aeroelastic solutions for a low-wing transonic transport model. There were two reasons that this approach was efficient: (1) The Euler flow solver with an interactive boundary layer required less computer time and storage than a Navier-Stokes solver, and (2) the simple plate technique required less time and storage and had a simpler interface with the flow solver, compared to a finite-element technique.

Both the computed viscous effect and the computed elastic effect were large. Each of these effects provided successively better comparisons with the experimental data. The objective of this research was achieved in that the simple accounting for static aeroelastic deformations greatly improved the viscous-flow wing pressure distributions. For the entire ranges of  $R_{\bar{c}}$  and  $q_\infty$ , the computational pressure distributions agreed well with experimental data. The computational results illustrated that  $R_{\bar{c}}$  and  $q_\infty$  had opposite effects on both the pressure distributions and lift coefficient. It must also be noted that the mechanisms associated with the  $R_{\bar{c}}$  and  $q_\infty$  effects on lift are fundamentally different; an increase in  $R_{\bar{c}}$  diminishes boundary-layer decambering effects (and thus increases lift) whereas an increase in  $q_\infty$  enhances

spanwise twist effects (and thus decreases lift). Thus, dynamic pressure effects can complicate wind-tunnel studies of Reynolds number effects if both are varied simultaneously. The magnitude of the computed elastic effect provided a measure of the influence of dynamic pressure which needs to be isolated whenever possible.

While the pressure distributions agreed well with National Transonic Facility (NTF) data, the lift coefficient was overpredicted. The overprediction was virtu-

ally constant through the  $R_c$  and  $q_\infty$  ranges and could be primarily a fuselage effect. However, small discrepancies in wing shock locations and pressure levels contributed to this overprediction. Where more accuracy is required, a Navier-Stokes calculation (without the approximate wing boundary layer and inviscid fuselage) would likely improve the results, especially at the lower Reynolds numbers. Also, more plates and calibration factors in the wing structural representation would likely result in some improvement, especially at the highest dynamic pressure.

## Appendix

This appendix provides a way (in the absence of any published user's manual) an Equivalent LAMinated Plate Solution (ELAPS) input file can be prepared for the structural representation of a wind-tunnel model wing as reported herein. Numerous ELAPS capabilities and alternate inputs are not addressed. The information is presented in the form of instructions based on the present structural representation in table A1. The wing is represented as plates made of solid materials subject to static loads. Each plate is defined by its planform, thickness distribution, camber distribution, and calibrated material properties.

The instructions in this appendix are directly related to the contents of the ELAPS input file in table A1. Each instruction beginning with "Enter" signifies a new line of input. Inputs from table A1 are often included in parentheses to help relate an instruction to a place in the table. All entries in a line are in free-field format; they have spaces between them but do not have to be in certain columns. All entries in a given line have to be included, even ones that do not relate to the present representation. Apostrophes enclose all alphanumeric data. Each number is entered in its proper form, integer or real.

The ELAPS code is used first with point-load calibration force data during the calibration, then with computed aerodynamic force data during the flow calculations. The last section of this appendix, "Concentrated Forces Revisited," addresses the procedure for changing the ELAPS input file and preparing an aerodynamic force data file before the flow calculation is started.

### Title

Enter 'TEXT' and the number of title lines (2).

Enter title lines, each with 80 characters or less including apostrophes.

('This is a structural representation of the Pathfinder I controls wing model.')

('This two-plate representation has calibration factors of 0.1165 and 0.4660.')

### Control Parameters

Enter 'CONTRL' and the unit number of a temporary scratch file (10).

Enter four numbers on one line:

1- controls amount of output in ELAPS output file (2)

2- selects a family of displacement polynomials for analysis (0)

3- selects static solver for analysis (2)

4- selects  $x$ - $y$  coordinate system for model input, 0 for global (0)

### Displacement Functions (Polynomials)

Enter 'NDFUN' and the number of displacement polynomials (3).

Enter numbers on one line for each displacement polynomial.

line 1:

identification number for  $x$ -direction displacement polynomial (11)

number of terms in  $x$  power series (4)

list of exponents for  $x$  power series (0 1 2 3)

number of terms in  $y$  power series (4)

list of exponents for  $y$  power series (2 3 4 5)

line 2:

identification number for  $y$ -direction displacement polynomial (22)

number of terms in  $x$  power series (4)

list of exponents for  $x$  power series (0 1 2 3)

number of terms in  $y$  power series (4)

list of exponents for  $y$  power series (1 2 3 4)

line 3:

identification number for  $z$ -direction displacement polynomial (33)

number of terms in  $x$  power series (4)

list of exponents for  $x$  power series (0 1 2 3)

number of terms in  $y$  power series (4)

list of exponents for  $y$  power series (2 3 4 5)

### Displacement Systems

Enter 'NDSYS' and the number of displacement systems (1).

Enter six numbers on one line:

1- identification number for displacement system (1234)

- 2- identification number for x-direction displacement polynomial (11)
- 3- identification number for y-direction displacement polynomial (22)
- 4- identification number for z-direction displacement polynomial (33)
- 5- pointer to a function that is not relevant but code reads an input value (0)
- 6- pointer to a function that is not relevant but code reads an input value (0)

The next two lines define a reference surface which surrounds the wing planform.

Enter three coordinates on one line for forward inboard corner of reference surface:

- 1- x coordinate, 0.0 is forward of entire wing representation (0.0)
- 2- y coordinate of most inboard point on wing representation (3.26)
- 3- z coordinate is zero (0.0)

Enter three coordinates on one line for rearward outboard corner of reference surface:

- 1- x coordinate of most rearward point on wing representation (38.51)
- 2- y coordinate of most outboard point on wing representation (26.48)
- 3- z coordinate is zero (0.0)

### **Material Properties**

Enter 'NMATL' and the number of calibrated regions (2).

For each calibration factor there is one calibrated region, for example one per plate.

Enter seven material numbers on one line for each calibrated region.

line 1:

- 1- Young's modulus in chordwise direction times calibration factor (3.169E+6)
- 2- Young's modulus in spanwise direction times calibration factor (3.169E+6)
- 3- Poisson's ratio (0.32)
- 4- shear modulus times calibration factor (1.200E+6)
- 5- density (0.288)
- 6- thermal coefficient that is not relevant but code reads an input value (0.0)
- 7- thermal coefficient that is not relevant but code reads an input value (0.0)

line 2:

- 1- Young's modulus in chordwise direction times calibration factor (12.675E+6)
- 2- Young's modulus in spanwise direction times calibration factor (12.675E+6)
- 3- Poisson's ratio (0.32)
- 4- shear modulus times calibration factor (4.800E+6)
- 5- density (0.288)
- 6- thermal coefficient that is not relevant but code reads an input value (0.0)
- 7- thermal coefficient that is not relevant but code reads an input value (0.0)

### **Structural Segments (Plates)**

Enter 'NSEGMT' and the number of plates (2).

Repeat 'PLATE' through 'SOLID' below for each plate, illustrated below for plate 1.

#### *Plate and displacement system identification*

Enter 'PLATE' and plate identification number (1).

Enter identification number of displacement system (1234).

#### *Planform geometry*

Enter 'PLANF' and same plate identification number as above (1).

The planform of a plate is defined by an inboard edge and an outboard edge.

Enter three inboard planform geometry numbers on one line:

- 1- x coordinate of most forward point on inboard edge of plate (20.03)
- 2- y coordinate of inboard edge of plate (3.26)
- 3- x coordinate of most rearward point on inboard edge of plate (31.14)

Enter three outboard planform geometry numbers on one line:

- 1- x coordinate of most forward point on outboard edge of plate (25.15)
- 2- y coordinate of outboard edge of plate (9.95)
- 3- x coordinate of most rearward point on outboard edge of plate (31.14)

### ***Thickness, referred to as depth***

Enter 'DEPTH' and same plate identification number as above (1).

Enter 'TABPTS' and 'XIETA'.

Enter two numbers on one line:

1- maximum exponent in chordwise direction for depth polynomial (6)

2- maximum exponent in spanwise direction for depth polynomial (1)

The following table defines inboard and outboard depth distributions.

Enter the number of lines in the following table (22) and 'XIETA' on one line.

Enter first half of lines in table with three inboard numbers on each line:

1- local normalized chordwise position inboard on plate, from 0.0 to 1.0

2- local normalized spanwise position inboard on plate (0.0)

3- dimensional inboard depth, if 0.0000 use 0.0001 on first and/or last line

Enter last half of lines in table with three outboard numbers on each line:

1- local normalized chordwise position outboard on plate, from 0.0 to 1.0

2- local normalized spanwise position outboard on plate (1.0)

3- dimensional outboard depth, if 0.0000 use 0.0001 on first and/or last line

### ***Camber***

Enter 'CAMBR' and same plate identification number as above (1).

Enter 'TABPTS' and 'XIETA'.

Enter two numbers on one line:

1- maximum exponent in chordwise direction for camber polynomial (6)

2- maximum exponent in spanwise direction for camber polynomial (1)

The following table defines inboard and outboard camber distributions.

Enter the number of lines in the following table (22) and 'XIETA'.

Enter first half of lines in table with three inboard numbers on each line:

1- local normalized chordwise position inboard on plate, from 0.0 to 1.0

2- local normalized spanwise position inboard on plate (0.0)

3- dimensional inboard camber

Enter last half of lines in table with three outboard numbers on each line:

1- local normalized chordwise position outboard on plate, from 0.0 to 1.0

2- local normalized spanwise position outboard on plate (1.0)

3- dimensional outboard camber

### ***Solid interior***

Enter 'SOLID' and same plate identification number as above (1).

Enter two numbers on one line:

1- solid material identification number (1)

2- angle of material axis in degrees (0.0)

### **Concentrated Forces**

Enter 'NFORC' and the number of force data sets (1).

Enter three numbers on one line:

1- identification number of load case (1)

2- identification number of displacement system (1234)

3- scale factor, not relevant but code reads an input value (1.0)

Enter two numbers on one line:

1- 15 for aerodynamic force data Fortran unit or 5 for calibration force data below (5)

2- form of alphanumeric force data, 1 is for free-field (1)

If 5 is on previous line the next two instructions apply; if 15, disregard them.

Enter number of calibration forces (1).

Enter five numbers on one line:

1- specifies direction in which force is acting, 3 is for z direction (3)

2- x location of force (35.55)

3- y location of force (23.60)

4- z location of force (0.0)

5- magnitude of force (155.0)

### **Static Analysis**

Enter 'STAT' and flag for static analysis (1).

Enter number of load cases (1).

## **Solution Vectors**

Enter 'OSOLTNV' and unit where solution vectors will be written out (21).

Enter three numbers on one line:

- 1- number of first load case to be written out (1)
- 2- number of last load case to be written out (1)
- 3- maximum exponent for solution vector coefficients (7)

## **Displacements**

Enter 'PDISP' and flag for displacement print out grid, 1 for same grid on all plates (1).

Enter two numbers on one line:

- 1- number of first load case to be printed out (1)
- 2- number of last load case to be printed out (1)

Enter two numbers on one line:

- 1- identification number of first plate to be printed (1)
- 2- identification number of last plate to be printed (2)

Enter two numbers on one line:

- 1- number of grid marks in streamwise direction on a plate (6)
- 2- number of grid marks in spanwise direction on a plate (6)

Enter two numbers on one line:

- 1- select coordinate system for grid points, 1 for nondimensional (1)
- 2- wing semispan used to nondimensionalize y (26.48)

## **End of Input Data**

Enter 'ENDDATA' and analysis flag, 1 to tell code to analyze input data (1).

## **Concentrated Forces Revisited**

The ELAPS code is used first with point-load calibration force data during the calibration and then with computed aerodynamic force data during the flow calculations. It is important that the user remembers to make the following change to the ELAPS input file before starting the flow calculations: in the second line under 'NFORC', a 5 becomes a 15 and the next two lines (calibration force data) are deleted. In addition to the ELAPS input file, an aerodynamic force data file, fort.15 (Fortran unit 15), is required in the following free-field format.

Enter number of forces (number of grid cell faces on the model surface).

Enter five numbers on a line (one line for each force):

- 1- specifies direction in which force is acting, 3 is for z direction (3)
- 2- x location of force
- 3- y location of force
- 4- z location of force
- 5- magnitude of force

Table A1. ELAPS Input File

```

'TEXT' 2
'This is a structural representation of the Pathfinder I controls wing model.'
'This two-plate representation has calibration factors of 0.1165 and 0.4660.'
'CONTRL' 10
  2 0 2 0
'NDFUN' 3
  11 4 0 1 2 3 4 2 3 4 5
  22 4 0 1 2 3 4 1 2 3 4
  33 4 0 1 2 3 4 2 3 4 5
'NDSYS' 1
  1234 11 22 33 0 0
  0.0 3.26 0.0
  38.51 26.48 0.0
'NMATL' 2
  3.169E+6 3.169E+6 0.32 1.200E+6 0.288 0.0 0.0
  12.675E+6 12.675E+6 0.32 4.800E+6 0.288 0.0 0.0
'NSEGMT' 2
  'PLATE' 1
    1234
    'PLANF' 1
      20.03 3.26 31.14
      25.15 9.95 31.14
    'DEPTH' 1
    'TABPTS' 'XIETA'
      6 1
        22 'XIETA'
0.000000 0.0 0.000100
0.100000 0.0 1.155980
0.200000 0.0 1.476374
0.300000 0.0 1.588386
0.400000 0.0 1.548475
0.500000 0.0 1.391178
0.600000 0.0 1.154536
0.700000 0.0 0.848852
0.800000 0.0 0.504587
0.900000 0.0 0.203231
1.000000 0.0 0.067129
0.000000 1.0 0.000100
0.100000 1.0 0.579257
0.200000 1.0 0.713137
0.300000 1.0 0.770764
0.400000 1.0 0.778338
0.500000 1.0 0.734894
0.600000 1.0 0.634576
0.700000 1.0 0.476123
0.800000 1.0 0.294958
0.900000 1.0 0.132017
1.000000 1.0 0.050310
  'CAMBR' 1
  'TABPTS' 'XIETA'

```



Table A1. Continued

6	1		
	22	'XIETA'	
0.000000	0.0	-1.779875	
0.100000	0.0	-1.877515	
0.200000	0.0	-1.936065	
0.300000	0.0	-1.999703	
0.400000	0.0	-2.066415	
0.500000	0.0	-2.122307	
0.600000	0.0	-2.157336	
0.700000	0.0	-2.163451	
0.800000	0.0	-2.156121	
0.900000	0.0	-2.183591	
1.000000	0.0	-2.312187	
0.000000	1.0	-1.303265	
0.100000	1.0	-1.305529	
0.200000	1.0	-1.311070	
0.300000	1.0	-1.313804	
0.400000	1.0	-1.311526	
0.500000	1.0	-1.304487	
0.600000	1.0	-1.286823	
0.700000	1.0	-1.259643	
0.800000	1.0	-1.244009	
0.900000	1.0	-1.264108	
1.000000	1.0	-1.355747	
	'SOLID'	1	
	1	0.0	
	'PLATE'	2	
	1234		
	'PLANF'	2	
	25.15	9.95	31.14
	35.44	26.48	38.51
	'DEPTH'	2	
	'TABPTS'	'XIETA'	
	6	1	
	22	'XIETA'	
0.000000	0.0	0.000100	
0.100000	0.0	0.579257	
0.200000	0.0	0.713137	
0.300000	0.0	0.770764	
0.400000	0.0	0.778338	
0.500000	0.0	0.734894	
0.600000	0.0	0.634576	
0.700000	0.0	0.476123	
0.800000	0.0	0.294958	
0.900000	0.0	0.132017	
1.000000	0.0	0.050310	
0.000000	1.0	0.000100	
0.100000	1.0	0.226508	
0.200000	1.0	0.292779	
0.300000	1.0	0.322255	

Table A1. Concluded

```

0.400000  1.0    0.323044
0.500000  1.0    0.302189
0.600000  1.0    0.255510
0.700000  1.0    0.190078
0.800000  1.0    0.115489
0.900000  1.0    0.050855
1.000000  1.0    0.015820
  'CAMBR'  2
  'TABPTS'  'XIETA'
    6      1
      22    'XIETA'
0.000000  0.0   -1.303265
0.100000  0.0   -1.305529
0.200000  0.0   -1.311070
0.300000  0.0   -1.313804
0.400000  0.0   -1.311526
0.500000  0.0   -1.304487
0.600000  0.0   -1.286823
0.700000  0.0   -1.259643
0.800000  0.0   -1.244009
0.900000  0.0   -1.264108
1.000000  0.0   -1.355747
0.000000  1.0    0.122927
0.100000  1.0    0.131148
0.200000  1.0    0.150428
0.300000  1.0    0.173564
0.400000  1.0    0.197272
0.500000  1.0    0.219426
0.600000  1.0    0.248908
0.700000  1.0    0.278250
0.800000  1.0    0.301556
0.900000  1.0    0.306203
1.000000  1.0    0.270532
  'SOLID'  2
    2  0.0
'NFORC'  1
  1  1234  1.0
  5  1
  1
  3  35.55  23.60  0.0  155.0
'STAT'  1
  1
'OSOLTNV' 21
  1  1  7
'PDISP'  1
  1  1
  1  2
  6  6
  1  26.48
'ENDDATA' 1

```

## References

1. Bisplinghoff, R. L.; Ashley, H.; and Halfman, R. L.: *Aeroelasticity*. Cambridge: Addison-Wesley Publishing Co., Inc., 1955.
2. Fung, Y. C.: *An Introduction to the Theory of Aeroelasticity*. New York: Dover Publications, Inc., 1993.
3. Giles, G. L.: *Equivalent Plate Analysis of Aircraft Wing Box Structures With General Planform Geometry*. AIAA-86-0940, 1986.
4. Giles, G. L.: *Further Generalization of an Equivalent Plate Representation for Aircraft Structural Analysis*. *J. of Aircraft*, vol. 26, 1989, pp. 67–74.
5. Cavallo, P. A.: *Coupling Static Aeroelastic Predictions With an Unstructured-Grid Euler/Interacting Boundary Layer Method*. M.Sc. Thesis, The George Washington University, July 1995.
6. Smith, W. D.: *Improved Pressure and Lift Predictions in Transonic Flow Using an Unstructured Mesh Euler Method With an Interacting Boundary Layer*. M.Sc. Thesis, The George Washington University, July 1994.
7. Jacobs, P. F.; and Gloss, B. B.: *Longitudinal Aerodynamic Characteristics of a Subsonic, Energy-Efficient Transport Configuration in the National Transonic Facility*. NASA TP-2922, 1989.
8. Al-Saadi, J. A.: *Analysis of Aircraft Configurations Using an Unstructured-Grid Euler Method With Interacting Boundary Layer on Lifting Surfaces*. NASA CDTP-1010, 1997.
9. Pirzadeh, S.: *Recent Progress in Unstructured Grid Generation*. AIAA -92-0445, Jan. 1992.
10. Lohner, R.; and Parikh, P.: *Generation of Three-Dimensional Unstructured Grids by the Advancing Front Method*. *Int'l. J. of Numerical Methods in Fluids*, vol. 8, 1988, pp. 1135–1149.
11. Samareh-Abolhassani, J.: *Unstructured Grids on NURBS Surfaces*. AIAA-93-3454, Aug. 1993.
12. Frink, N. T.: *Recent Progress Toward a Three-Dimensional Unstructured Navier-Stokes Flow Solver*. AIAA-94-0061, Jan. 1994.
13. Frink, N. T.: *Upwind Scheme for Solving the Euler Equations on Unstructured Tetrahedral Meshes*. *AIAA J.*, vol. 30, no. 1, Jan. 1992, pp. 70–77.
14. Roe, P. L.: *Characteristic Based Schemes for the Euler Equations*. *Annual Review of Fluid Mechanics*, vol. 18, 1986, pp. 337–365.
15. Al-Saadi, J. A.; and Smith, W. D.: *Analysis of a Supercritical Wing With a Blunt Trailing Edge Using an Unstructured-Grid Euler Method*. NASA TM-4688, 1995.
16. Cebeci, T.; Clark, R. W.; Chang, K. C.; Halsey, N. D.; and Lee, K.: *Airfoils With Separation and the Resulting Wakes*. *J. of Fluid Mech.*, vol. 163, 1986, pp. 323–347.
17. Chen, L. T.; and Bui, M. N.: *An Interactive Scheme for Transonic Wing/Body Flows Based on Euler and Inverse Boundary-Layer Equations*. AIAA-90-1586, June 1990.
18. Cebeci, T.; and Bradshaw, P.: *Physical and Computational Aspects of Convective Heat Transfer*. Springer-Verlag, 1984.
19. Cook, R. D.; Malkus, D. S.; and Plesha, M. E.: *Concepts and Applications of Finite Element Analysis*. John Wiley & Sons, Inc., 1989.
20. Parikh, P.: *Development of a Modular Aerodynamic Design System Based on Unstructured Grids*. AIAA-97-0172, Jan. 6–10, 1997.
21. Batina, J. T.: *Unsteady Euler Algorithm With Unstructured Dynamic Mesh for Complex-Aircraft Aerodynamic Analysis*. *AIAA J.*, vol. 29, 1991, pp. 327–333.
22. Mineck, R. E.: *Reynolds Number Effects on the Performance of Lateral Control Devices*. NASA TM-2000-210541, 2000.
23. Fuller, D. E.: *Guide for Users of the National Transonic Facility*. NASA TM-83124, 1981.
24. Foster, J. M.; and Adcock, J. B.: *User's Guide for the National Transonic Facility Data System*. NASA TM-100511, 1987.
25. Chan, Y. Y.: *Comparison of Boundary Layer Trips of Disks and Grit Types on Airfoil Performance at Transonic Speeds*. NAE-AN-56 (NRC-29908), National Aeronautical Establishment (Ottawa, Ontario), Dec., 1988.
26. Coleman, H. W.; and Steele, W. G., Jr.: *Experimentation and Uncertainty Analysis for Engineers*. John Wiley & Sons, Inc., 1989.
27. Wahls, R. A.; Adcock, J. B.; Witkowski, D. P.; and Wright, F. L.: *A Longitudinal Aerodynamic Data Repeatability Study for a Commercial Transport Model Test in the National Transonic Facility*. NASA TP-3522, 1995.

Table 1. Boundary-Layer Strip Locations

Station	$\eta$
1	1.140
2	0.275
3	0.375
4	0.509
5	0.630
6	0.790
7	0.922
8	0.979

Table 2. Material Properties for Vascomax T200®

Young's modulus, psi . . . . .	27 200 000
Shear modulus, psi . . . . .	10 300 000
Poisson's ratio. . . . .	0.320
Density, lb/in <sup>3</sup> . . . . .	0.288

Table 3. NTF Test 88 Conditions for Cases Calculated

Case, fig.	$M_\infty$	$\alpha$ , deg	$C_L$	$R_c \times 10^{-6}$	$q_\infty$ , psf	Test gas	Run	Point
1, 11	0.820	1.98	0.527	3	1052	Air	130	1761
2, 12	0.819	1.92	0.562	13	1091	N <sub>2</sub>	144	1933
3, 13	0.819	1.98	0.541	13	1736	N <sub>2</sub>	156	2094
4, 14	0.821	1.85	0.537	22	1788	N <sub>2</sub>	21	244
5, 15	0.820	1.93	0.527	22	2398	N <sub>2</sub>	12	122
6, 16	0.820	1.88	0.514	30	2429	N <sub>2</sub>	36	457

Table 4. Nominal Location for Lower Surface Orifices

$x/c$ for row at $\eta =$						
0.140	0.275	0.375	0.509	0.630	0.790	0.922
0.025	0.025	0.025	0.025	0.025	0.025	0.025
	0.050	0.050				
0.075	0.075	0.075	0.075	0.075	0.075	0.075
	0.100	0.100				
0.125	0.125	0.125	0.125	0.125	0.125	0.125
	0.150	0.150				
0.200	0.200	0.200	0.200	0.200	0.200	0.200
0.300	0.300	0.300	0.300	0.300	0.300	0.300
0.400	0.400	0.400	0.400	0.400	0.400	0.400
0.500	0.500	0.500	0.500	0.500	0.500	0.500
0.600	0.600	0.600	0.600	0.590	0.580	0.600
0.700	0.700	0.700	0.700	0.700	0.700	0.700
0.800	0.800	0.800	0.800	0.800	0.800	0.800
0.900	0.900	0.900	0.900	0.900	0.900	0.900
0.950	0.950	0.950	0.950	0.950	0.950	0.950
1.000	1.000	1.000	1.000	1.000	1.000	1.000

Table 5. Nominal Location for Upper Surface Orifices

$x/c$ for row at $\eta =$						
0.140	0.275	0.375	0.509	0.630	0.790	0.922
0.000	0.000	0.000	0.000	0.000	0.000	0.000
	0.025	0.025				
0.050	0.050	0.050	0.050	0.050	0.050	0.050
	0.075	0.075				
0.100	0.100	0.100	0.100	0.100	0.100	0.100
0.150	0.150	0.150	0.150	0.150	0.150	0.150
0.200	0.200	0.200	0.200	0.200	0.200	0.200
	0.250	0.250	0.250	0.250	0.250	0.250
0.300	0.300	0.300	0.300	0.300	0.300	0.300
	0.350	0.350	0.350	0.350	0.350	0.350
0.400	0.400	0.400	0.400	0.400	0.400	0.400
0.450	0.440	0.440	0.440	0.440	0.440	0.440
0.500	0.480	0.480	0.480	0.480	0.480	0.480
	0.520	0.520	0.520	0.520	0.520	0.520
0.550	0.560	0.560	0.560	0.560	0.560	0.560
0.600	0.600	0.600	0.600	0.600	0.600	0.600
0.640	0.640	0.640	0.640	0.640	0.640	0.640
0.680	0.680	0.680	0.680	0.670	0.680	0.680
0.720	0.720	0.720	0.715	0.695	0.730	0.730
	0.750			0.740	0.760	0.760
0.770	0.780	0.770	0.760	0.780	0.790	0.790
0.820	0.820	0.830	0.820	0.830	0.845	0.825
						0.855
0.880	0.880	0.880	0.880	0.880	0.875	0.890
					0.905	
0.940	0.940	0.949	0.940	0.940	0.950	0.940
1.000	1.000	1.000	1.000	1.000	1.000	1.000

Table 6. Computed Lift Coefficients, Their Differences, and Comparisons to Experiment

Case, fig.	$R_{\bar{c}} \times 10^{-6}$	$q_{\infty}$ , psf	Rigid-inviscid	Rigid-viscous	Elastic-viscous	NTF experiment	Viscous effect	Elastic effect	Difference from experiment
1, 11	3	1052	0.870	0.636	0.586	0.527	-0.234	-0.050	-0.059
2, 12	13	1091	0.856	0.679	0.621	0.562	-0.177	-0.058	-0.059
3, 13	13	1736	0.867	0.687	0.598	0.541	-0.180	-0.089	-0.057
4, 14	22	1788	0.849	0.687	0.591	0.537	-0.162	-0.096	-0.054
5, 15	22	2398	0.861	0.697	0.577	0.527	-0.164	-0.120	-0.050
6, 16	30	2429	0.852	0.700	0.573	0.514	-0.152	-0.127	-0.059

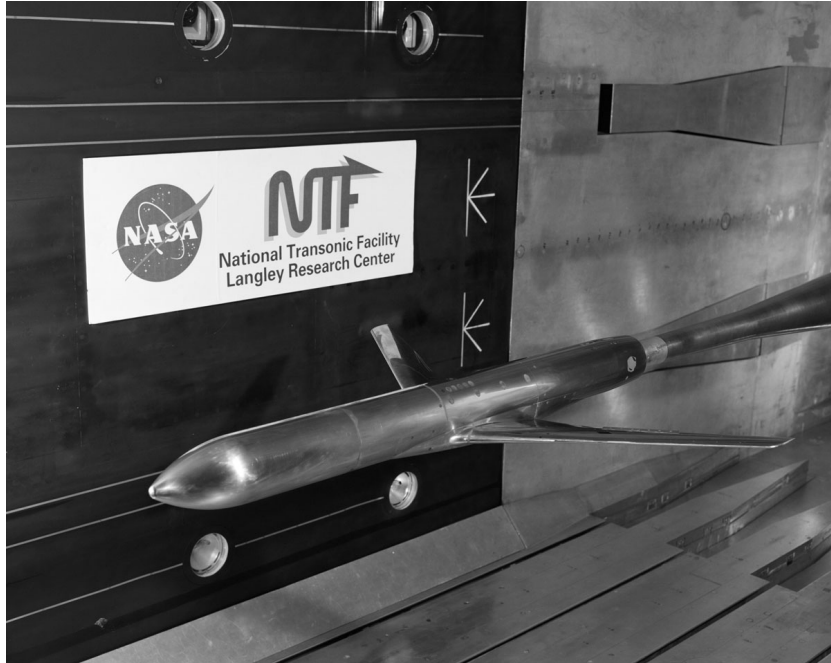


Figure 1. Wing-fuselage configuration of NTF Pathfinder-I lateral controls wing. Spoiler control surface is deflected in photograph.

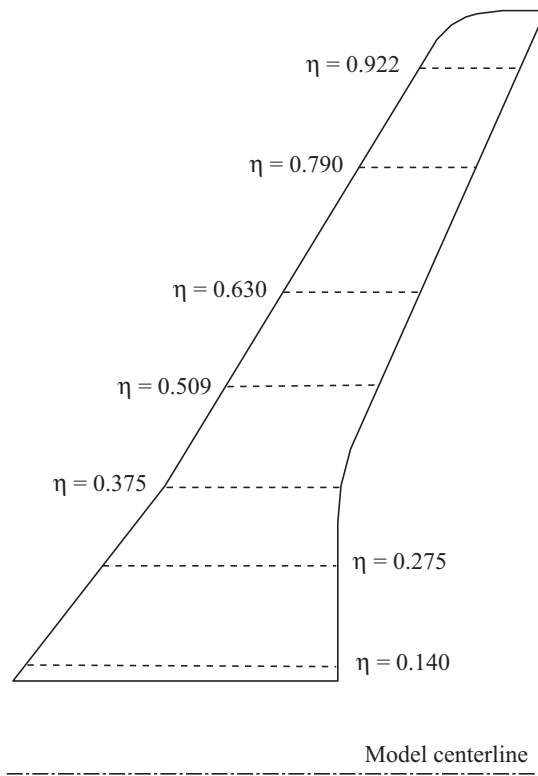


Figure 2. Wing planform sketch with pressure orifice rows.

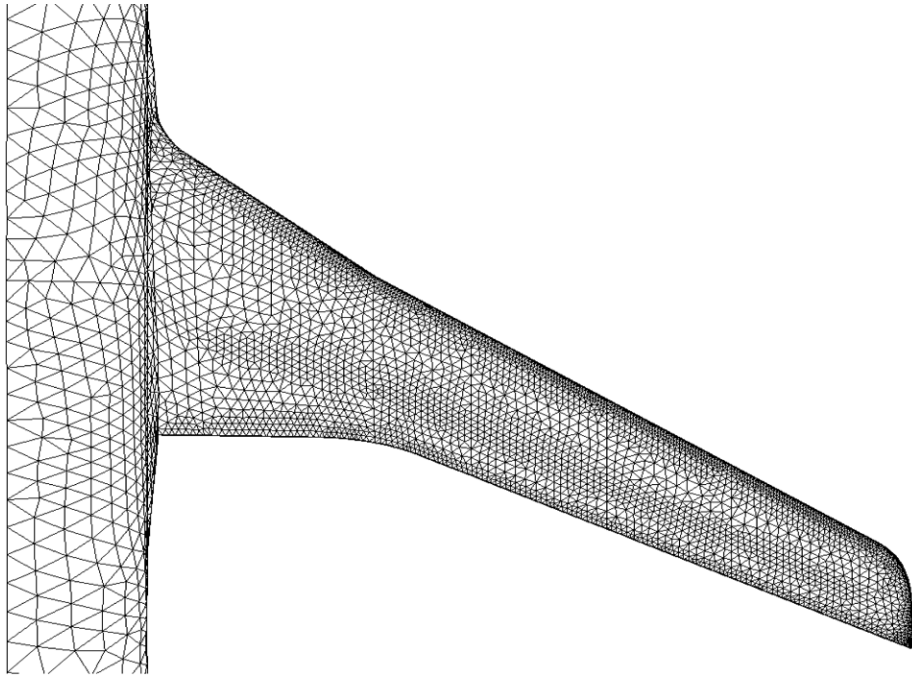


Figure 3. Surface mesh of wing upper surface.

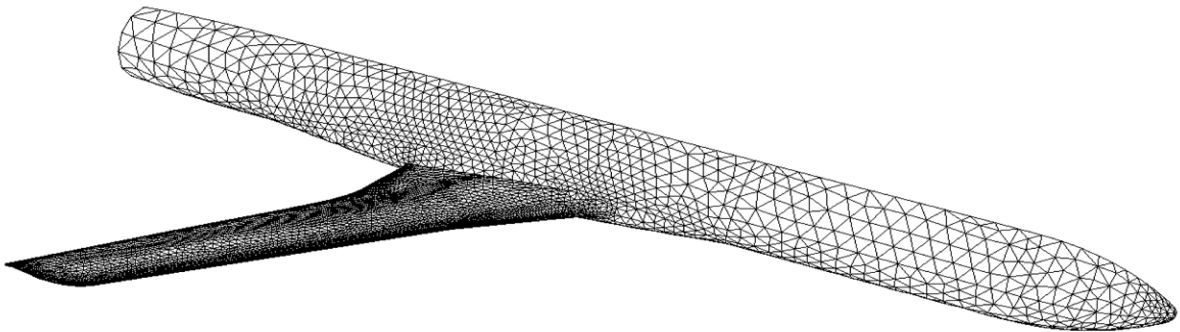


Figure 4. Surface mesh of complete grid.

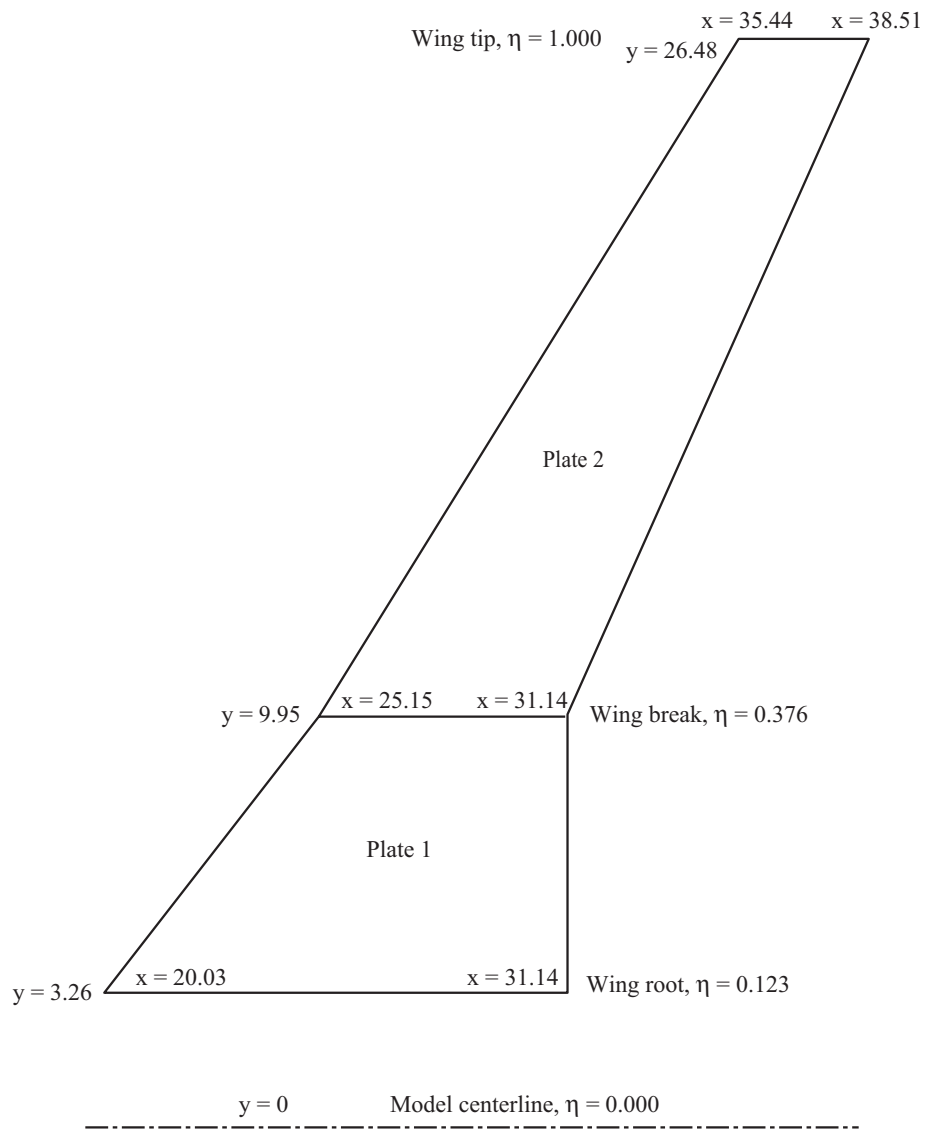


Figure 5. Plate representation of wing planform. Coordinates  $x$  and  $y$  are in inches, with origin located 10.5 in. aft of fuselage nose on model centerline.



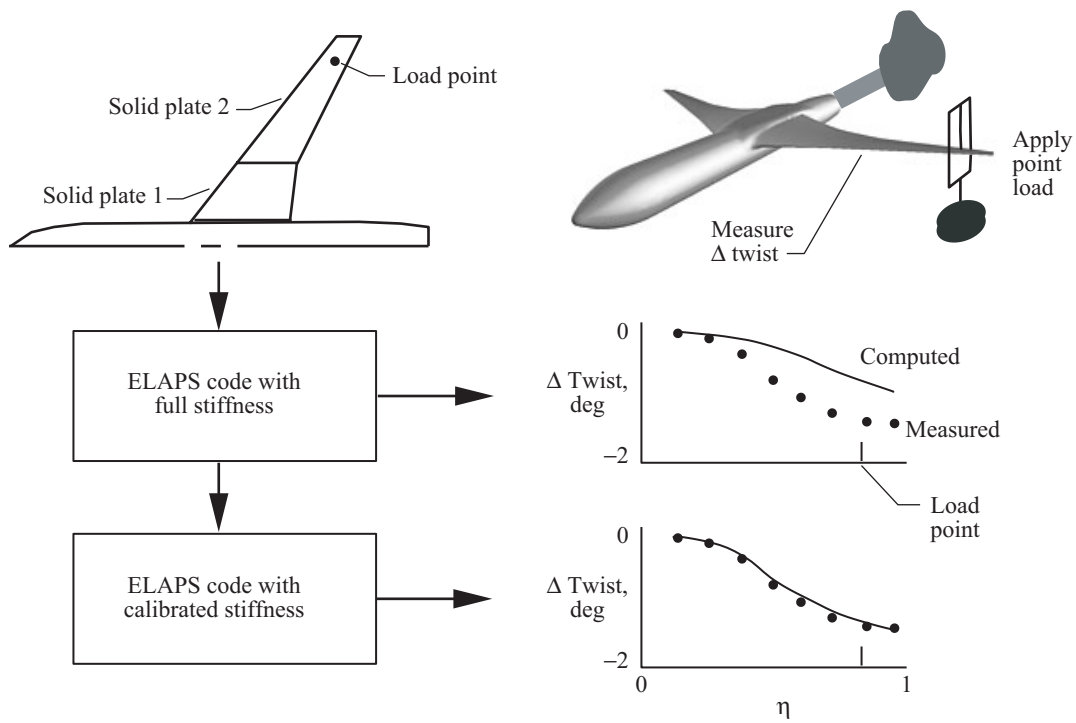


Figure 6. Procedure for calibration of structural representation.

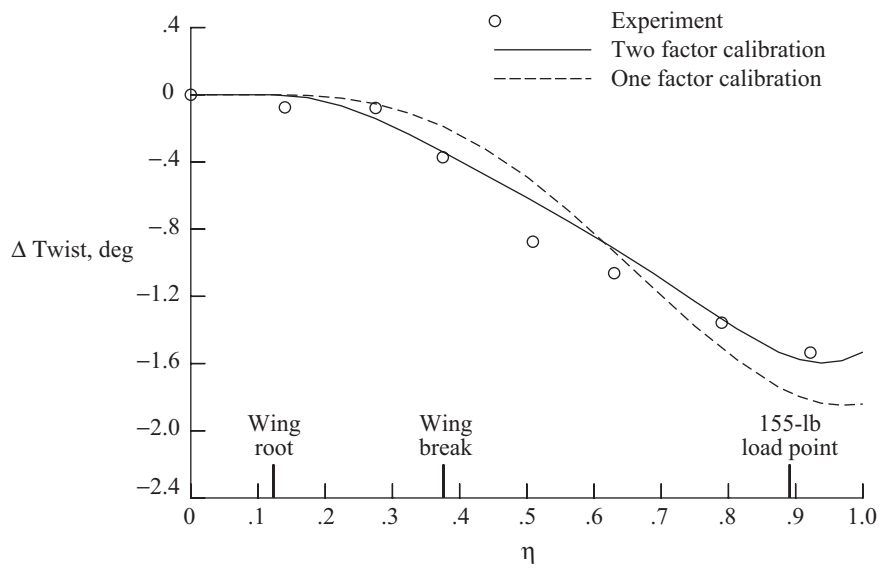


Figure 7. Static-loading wing-twist increment for calibration of input to ELAPS code.

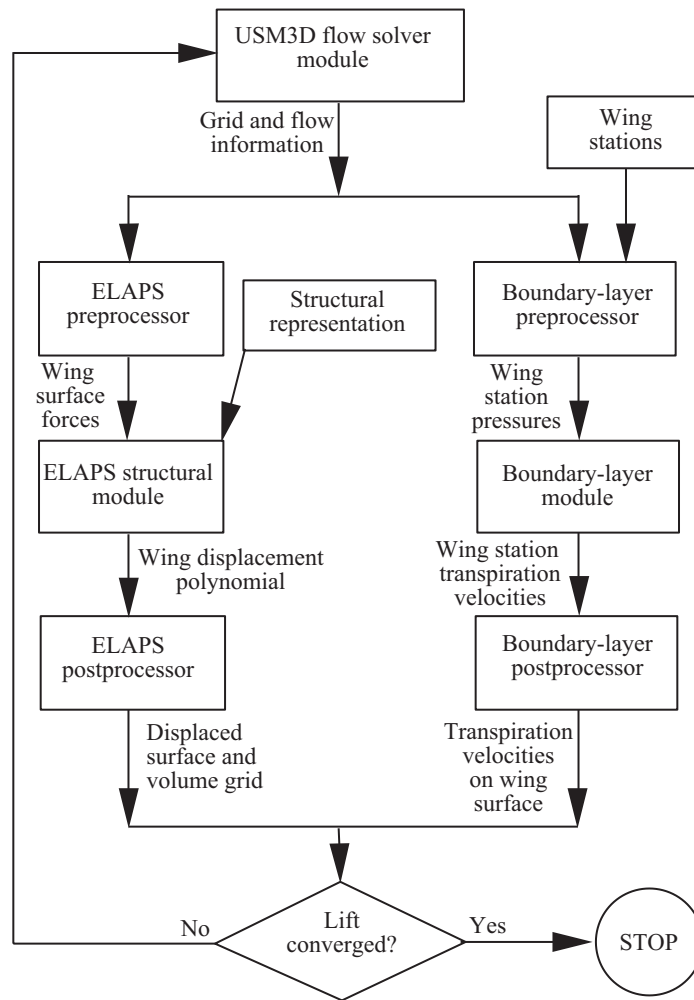


Figure 8. Flow chart of computational method.

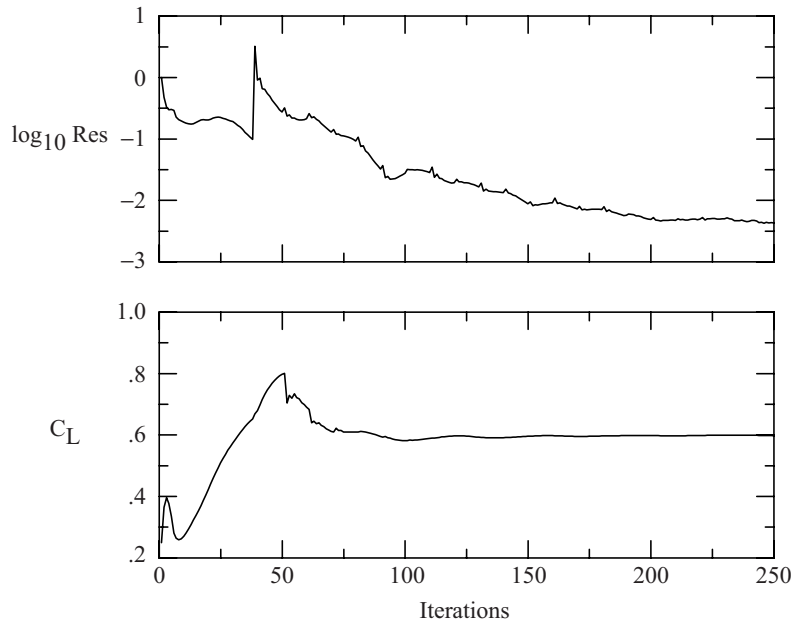


Figure 9. Typical converge history (wind-tunnel case 3,  $M_\infty = 0.819$ ;  $\alpha = 1.98^\circ$ ;  $R_c = 13.0 \times 10^6$ ;  $q_\infty = 1736$  psf).

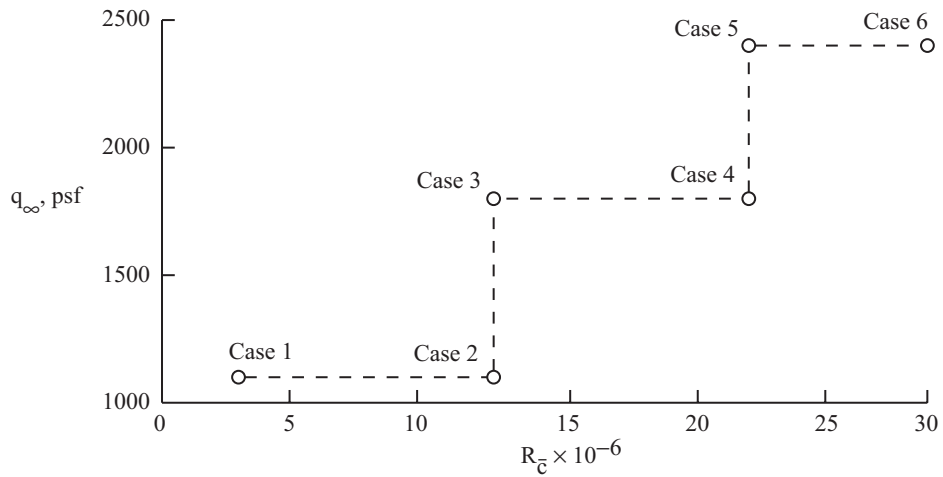


Figure 10. Nominal Reynolds numbers and dynamic pressures.

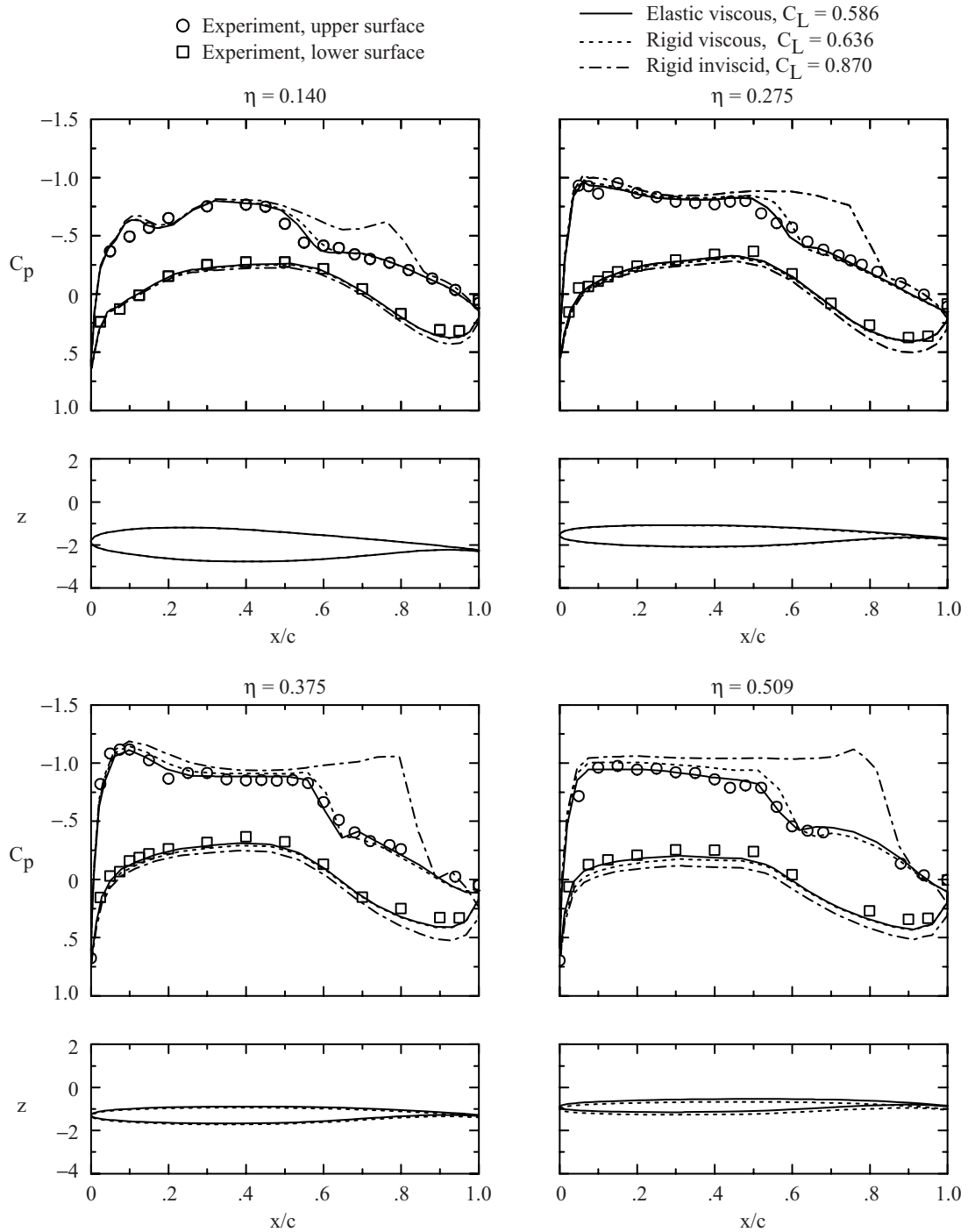


Figure 11. Wing pressure distributions and deformations for wind-tunnel case 1:  $M_\infty = 0.820$ ;  $\alpha = 1.98^\circ$ ;  $R_{\bar{c}} = 3 \times 10^6$ ;  $q_\infty = 1052$  psf;  $C_L = 0.527$ .

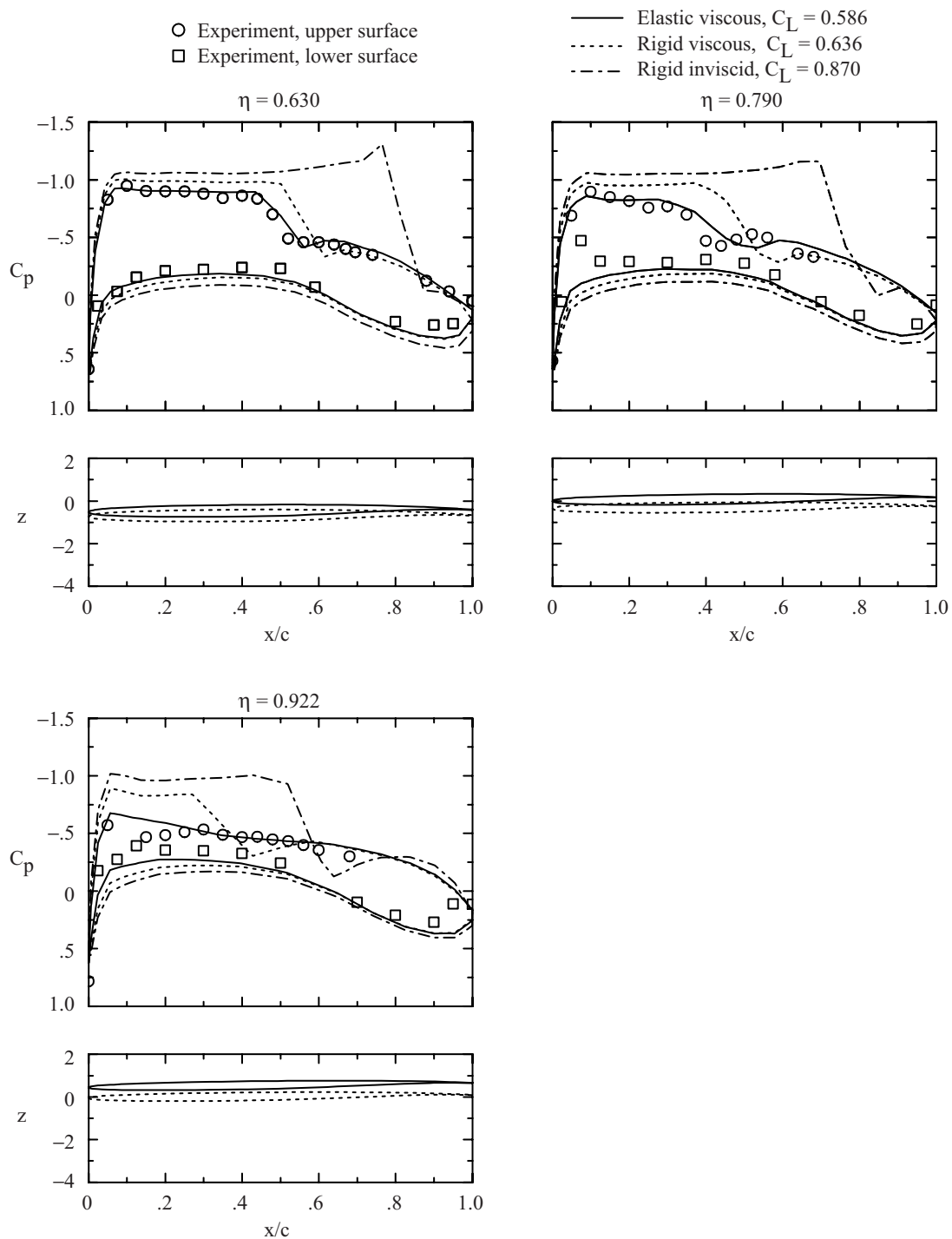


Figure 11. Concluded.

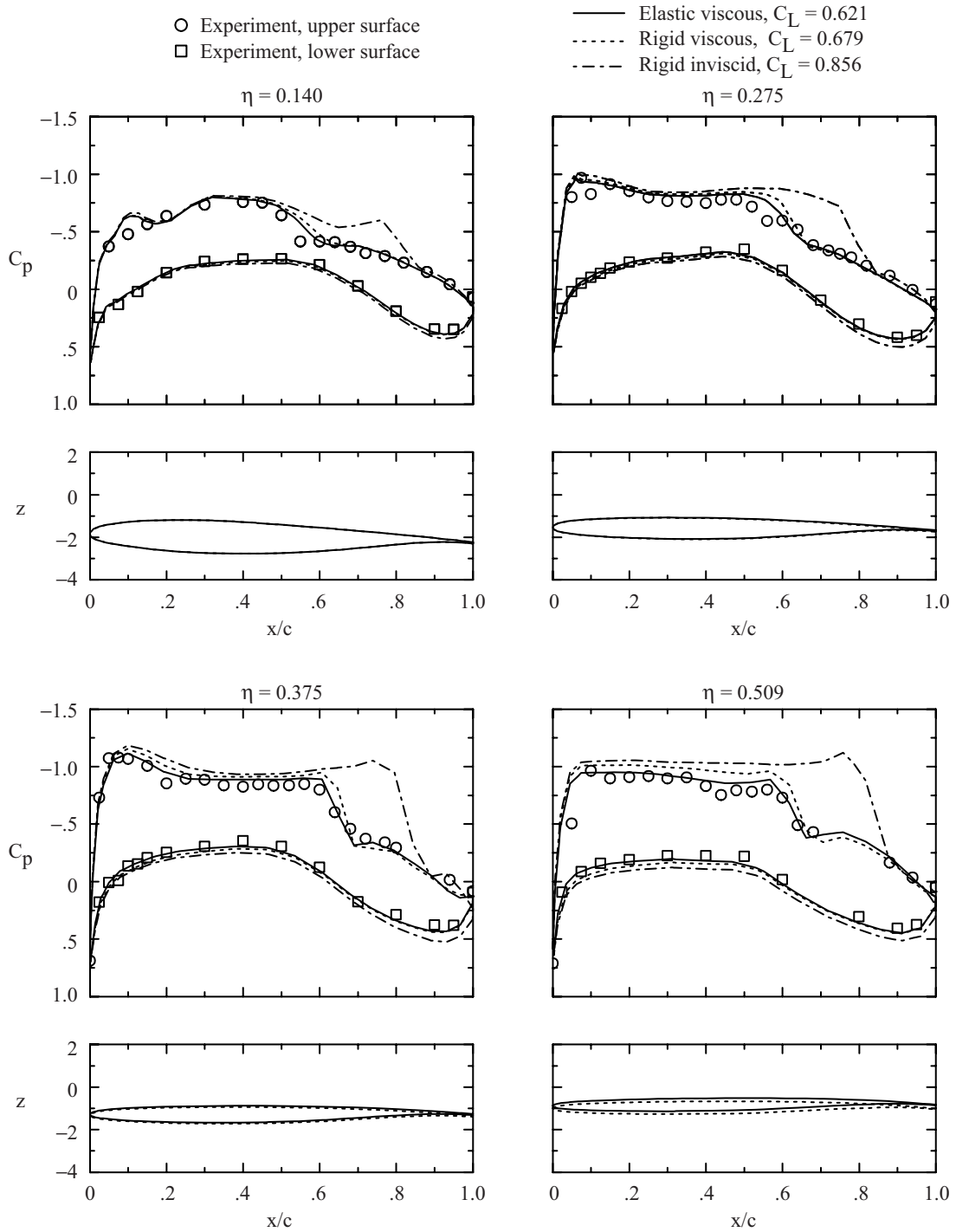


Figure 12. Wing pressure distributions and deformations for wind-tunnel case 2:  $M_\infty = 0.819$ ;  $\alpha = 1.92^\circ$ ;  $R_c = 13 \times 10^6$ ;  $q_\infty = 1091$  psf;  $C_L = 0.562$ .

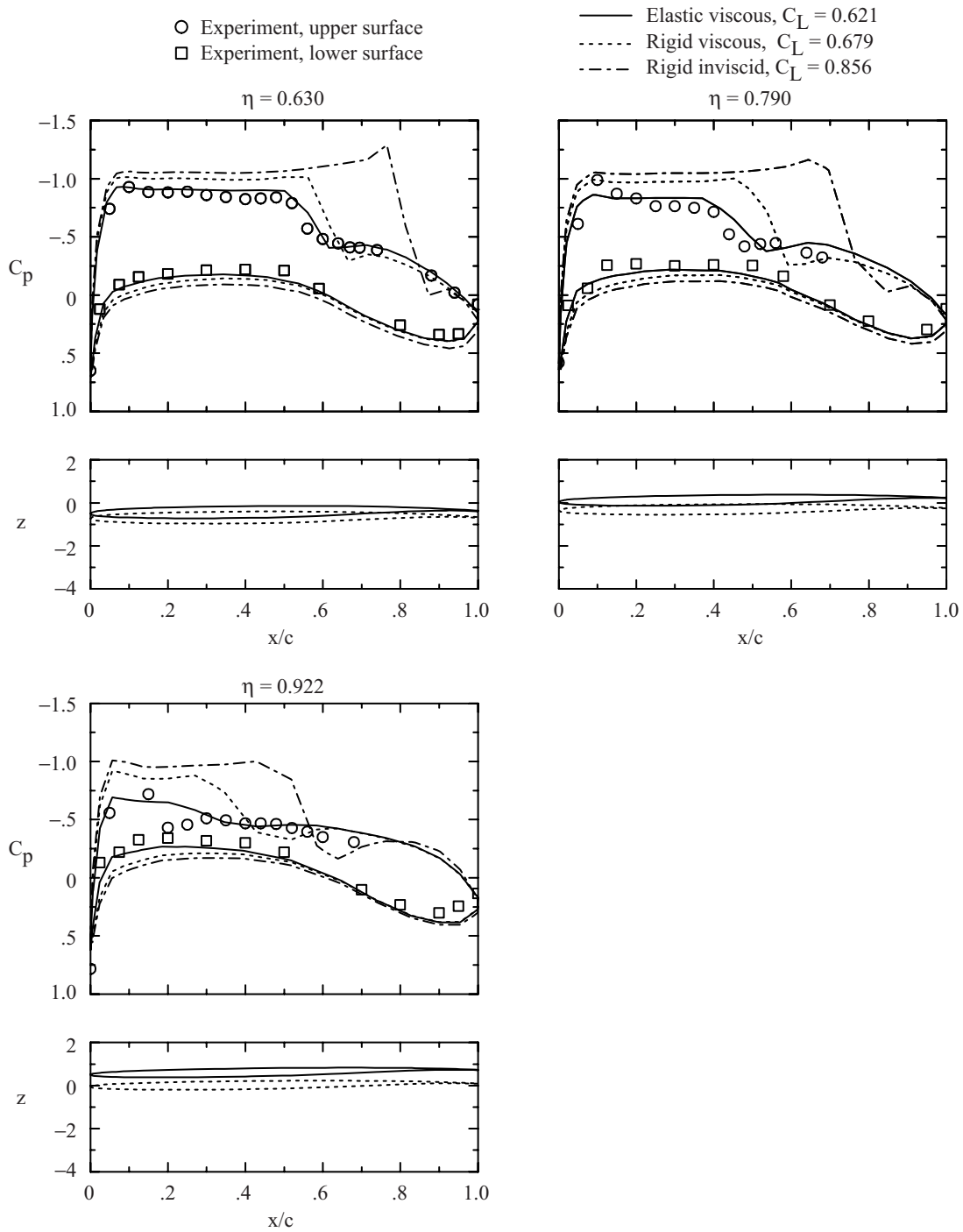


Figure 12. Concluded.

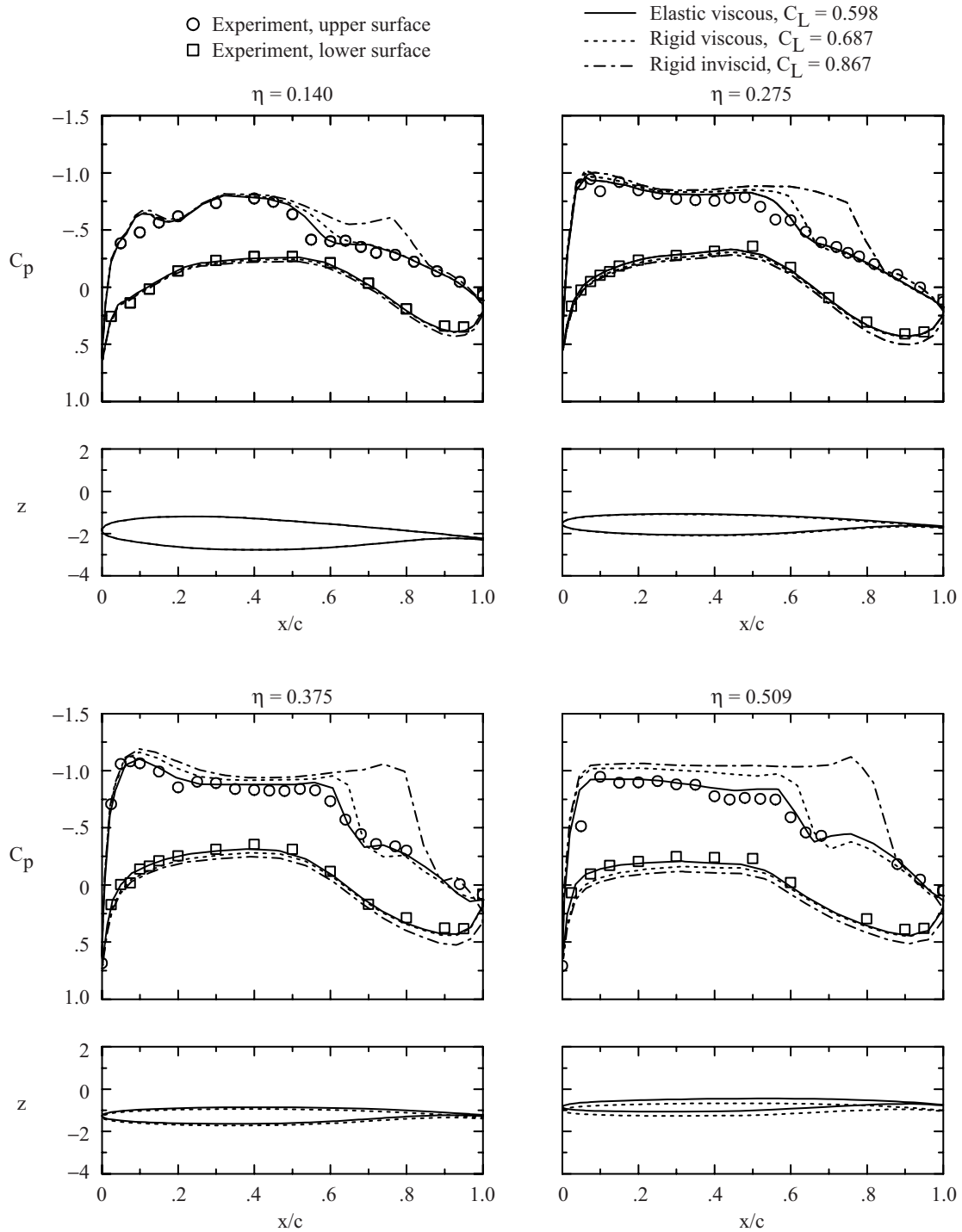


Figure 13. Wing pressure distributions and deformations for wind-tunnel case 3:  $M_\infty = 0.819$ ;  $\alpha = 1.98^\circ$ ;  $R_{\bar{c}} = 13 \times 10^6$ ;  $q_\infty = 1736$  psf;  $C_L = 0.541$ .



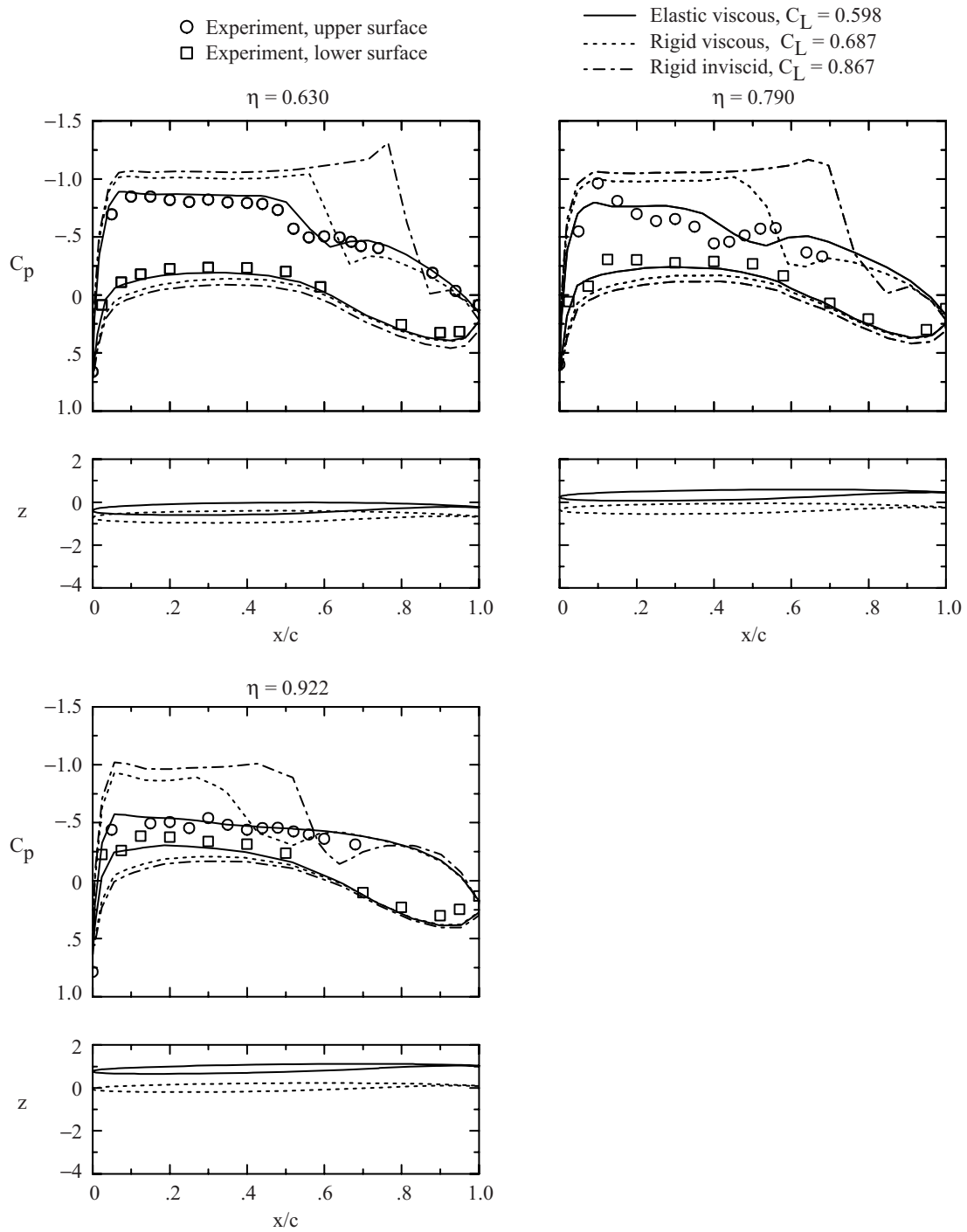


Figure 13. Concluded.

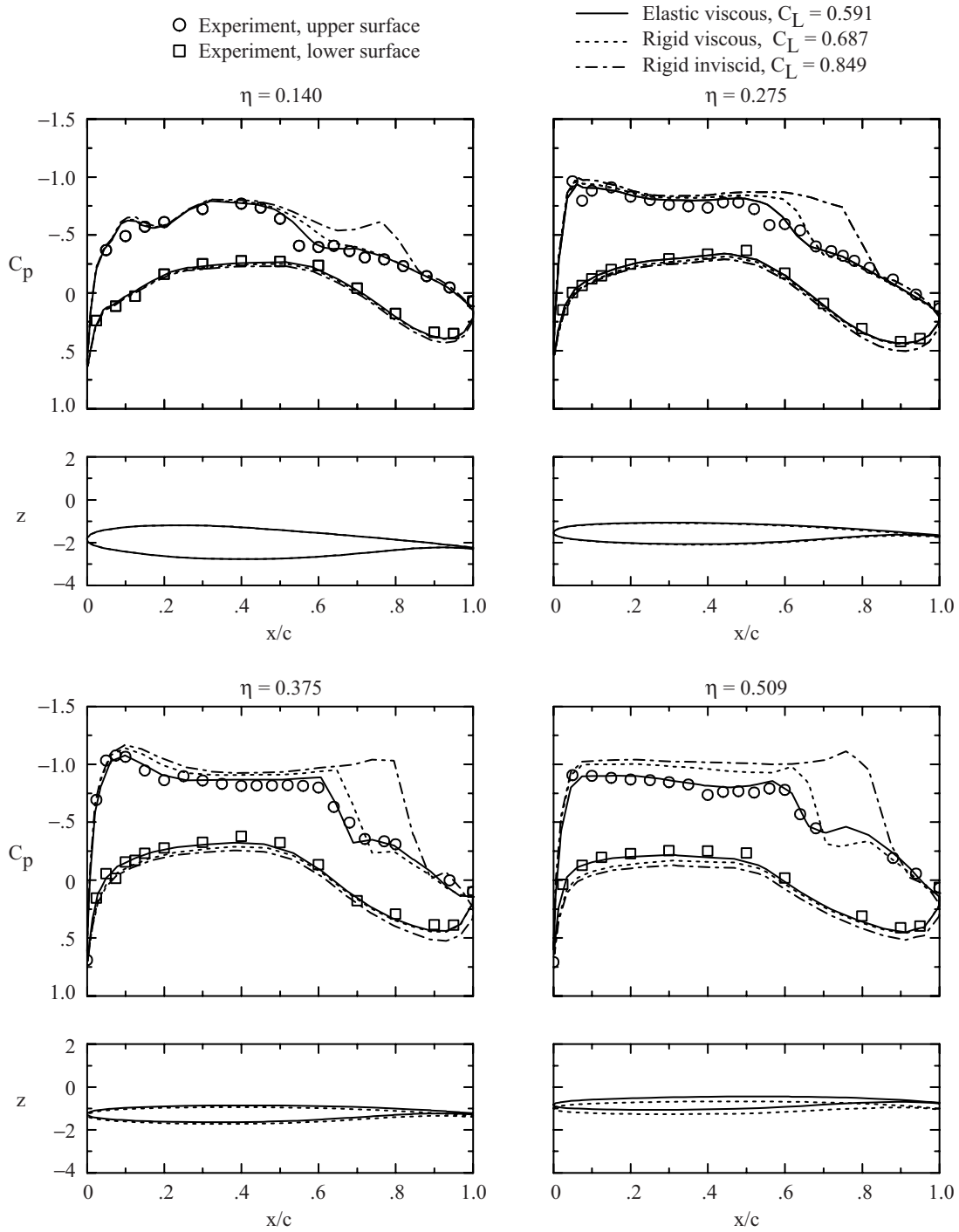


Figure 14. Wing pressure distributions and deformations for wind-tunnel case 4:  $M_\infty = 0.821$ ;  $\alpha = 1.85^\circ$ ;  $R_{\bar{c}} = 22 \times 10^6$ ;  $q_\infty = 1788$  psf;  $C_L = 0.537$ .

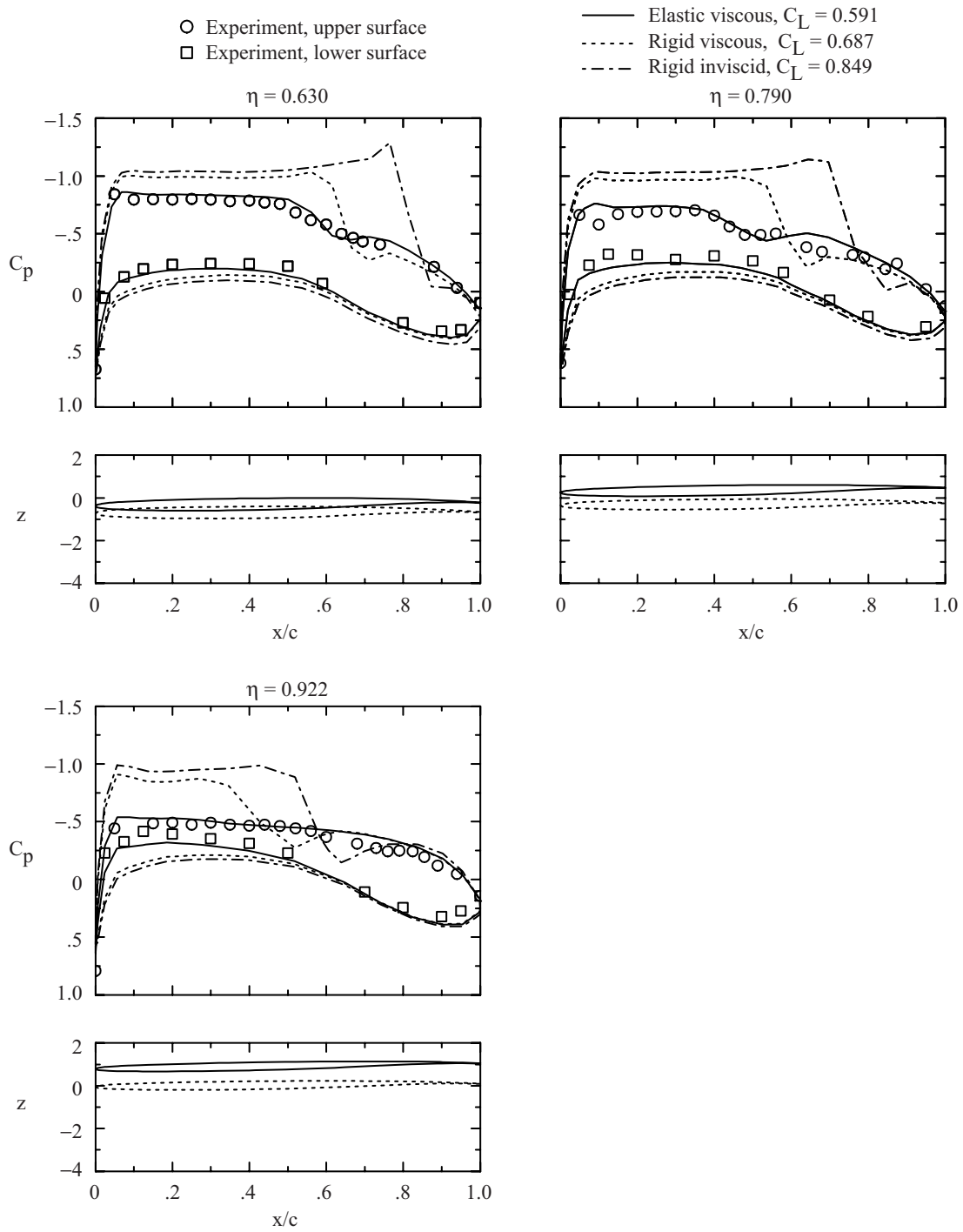


Figure 14. Concluded.

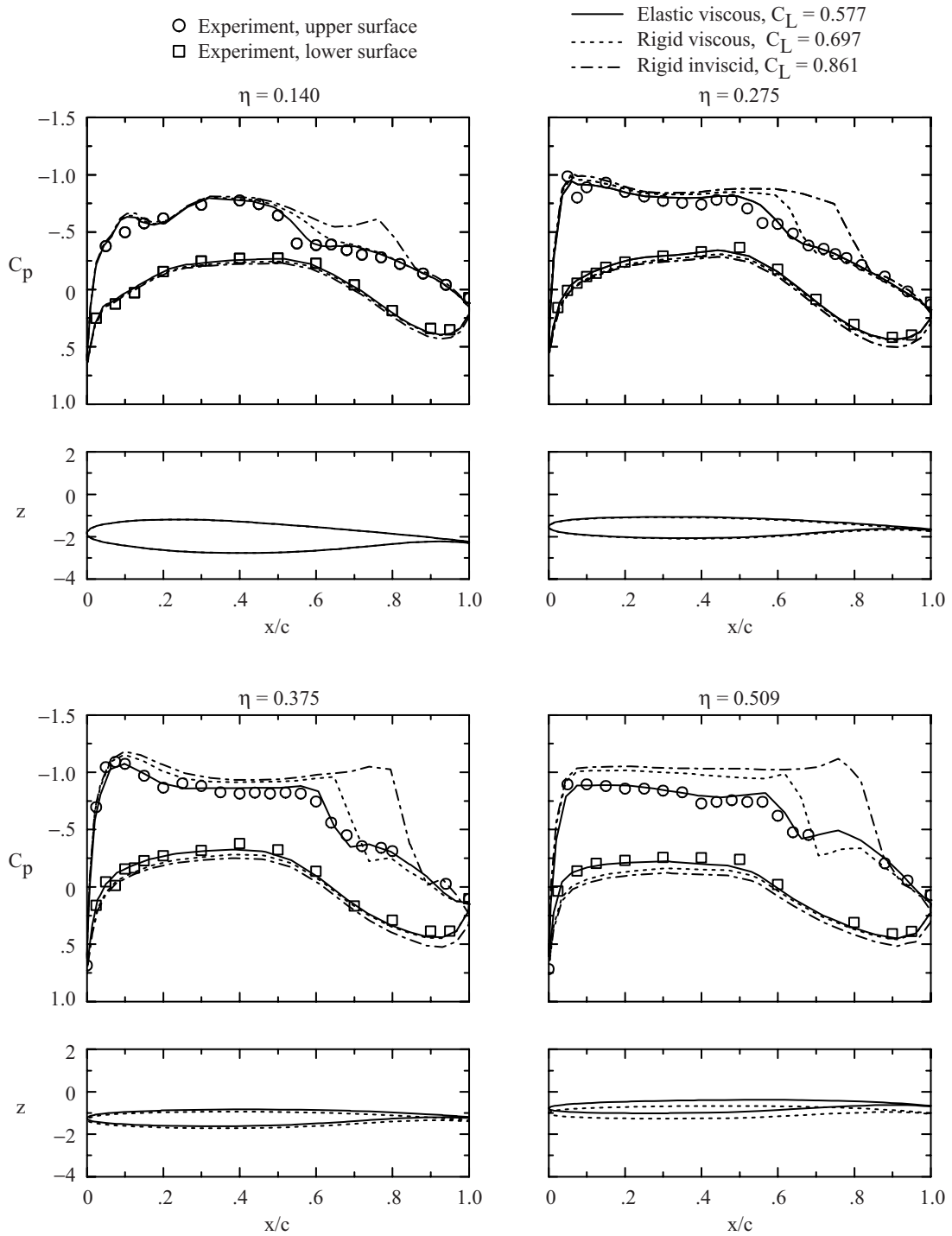


Figure 15. Wing pressure distributions and deformations for wind-tunnel case 5:  $M_\infty = 0.820$ ;  $\alpha = 1.93^\circ$ ;  $R_c = 22 \times 10^6$ ;  $q_\infty = 2398$  psf;  $C_L = 0.527$ .

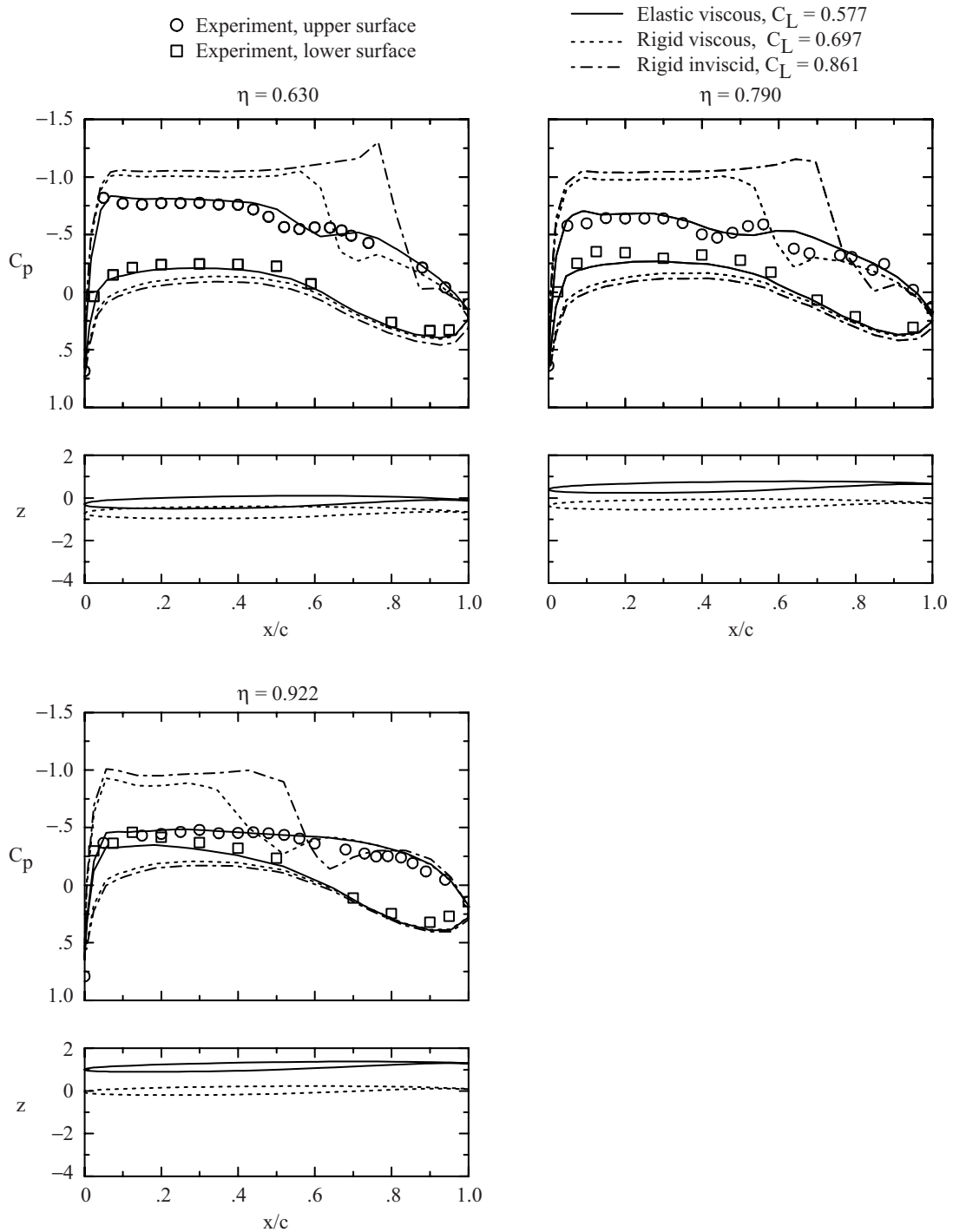


Figure 15. Concluded.

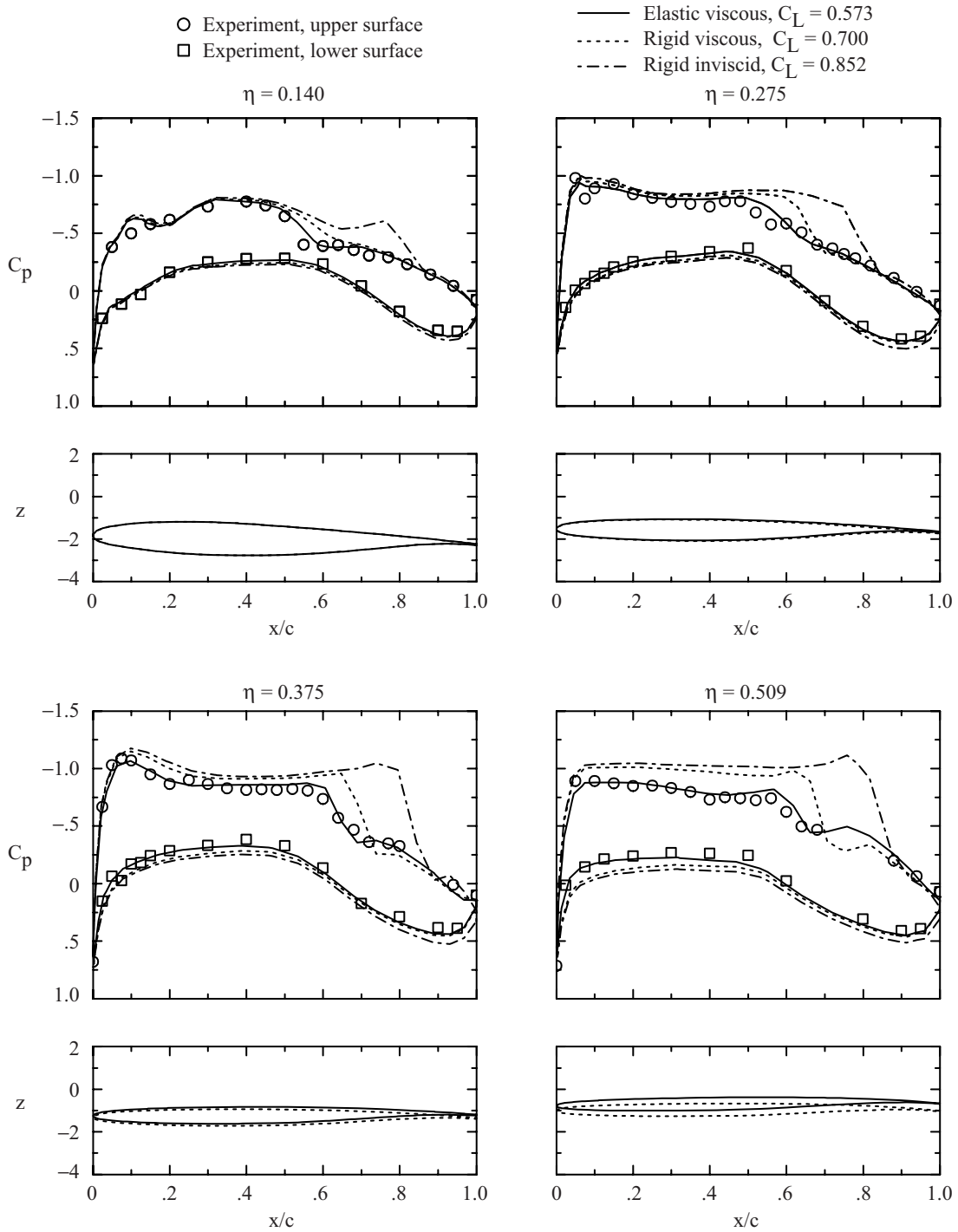


Figure 16. Wing pressure distributions and deformations for wind-tunnel case 6:  $M_\infty = 0.820$ ;  $\alpha = 1.88^\circ$ ;  $R_c = 30 \times 10^6$ ;  $q_\infty = 2429$  psf;  $C_L = 0.514$ .

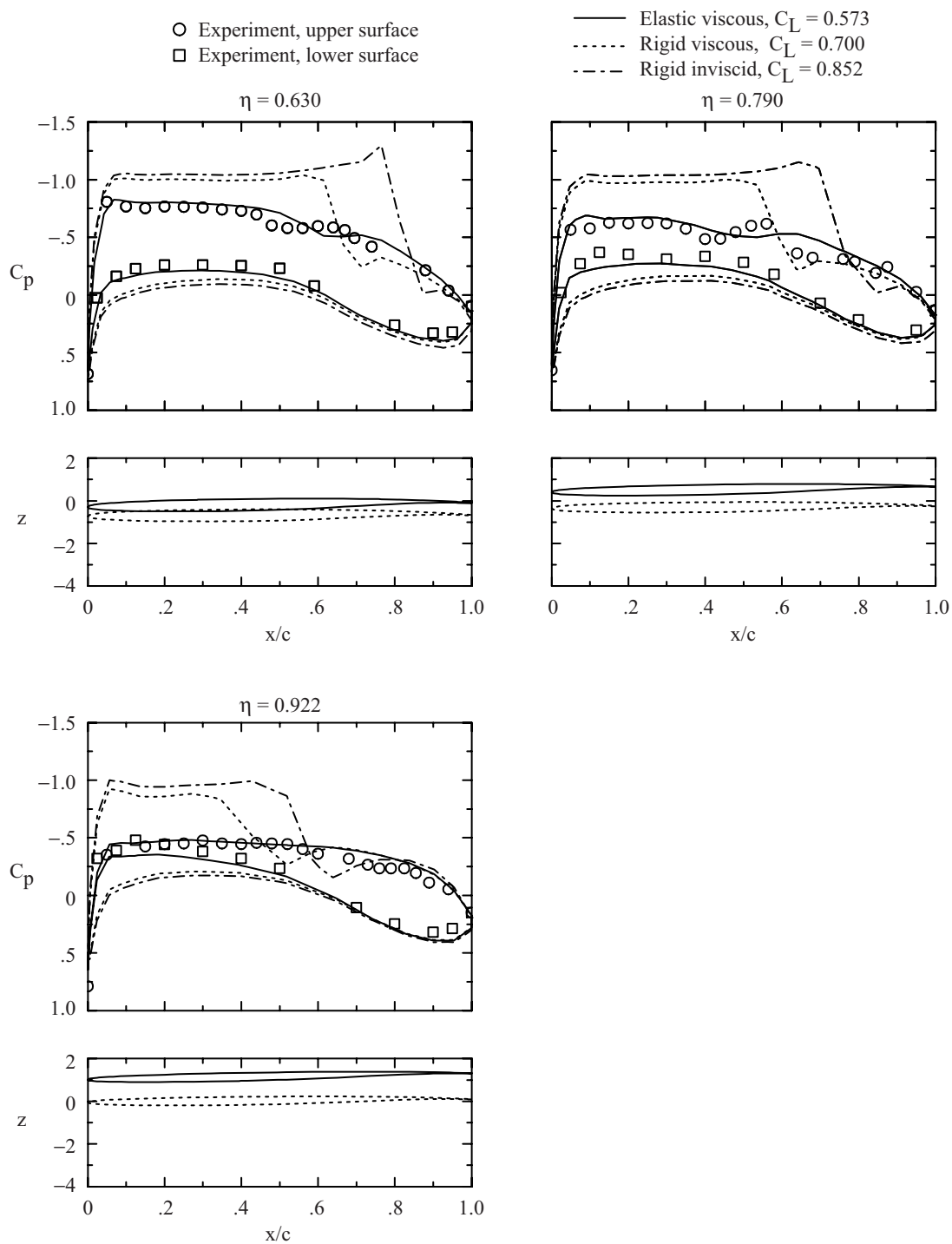


Figure 16. Concluded.

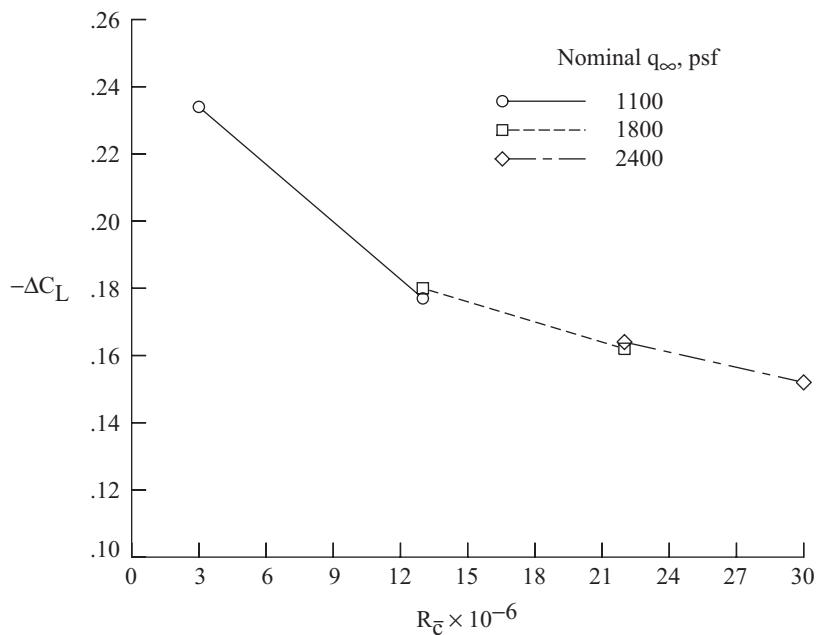


Figure 17. Effect of Reynolds number on computed viscous decrement in rigid-wing lift coefficient.

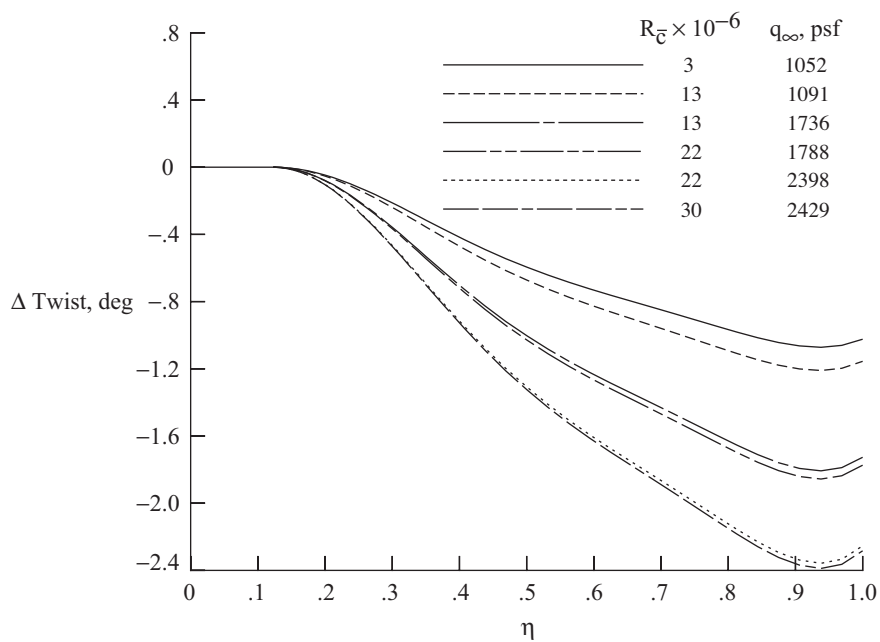


Figure 18. Computed wing-twist increment due to aerodynamic load for the six cases.



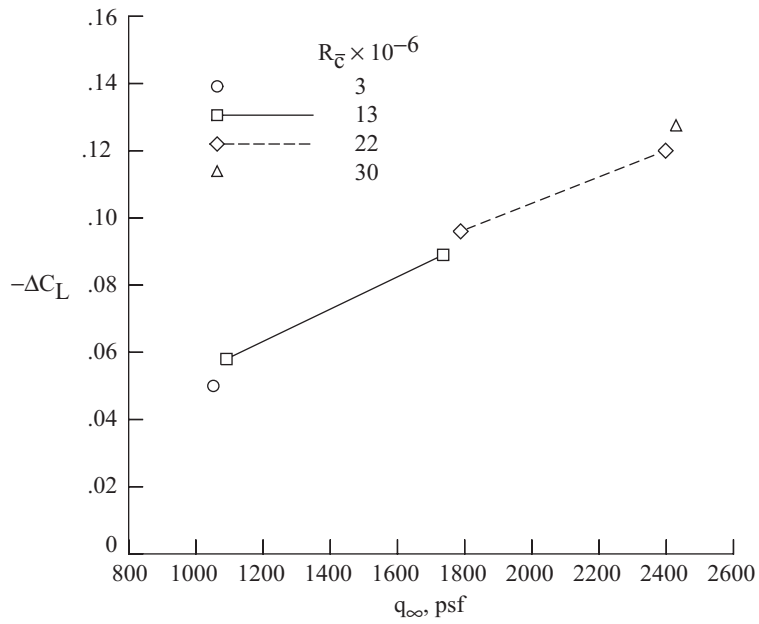


Figure 19. Effect of dynamic pressure on computed elastic decrement in viscous-flow lift coefficient.

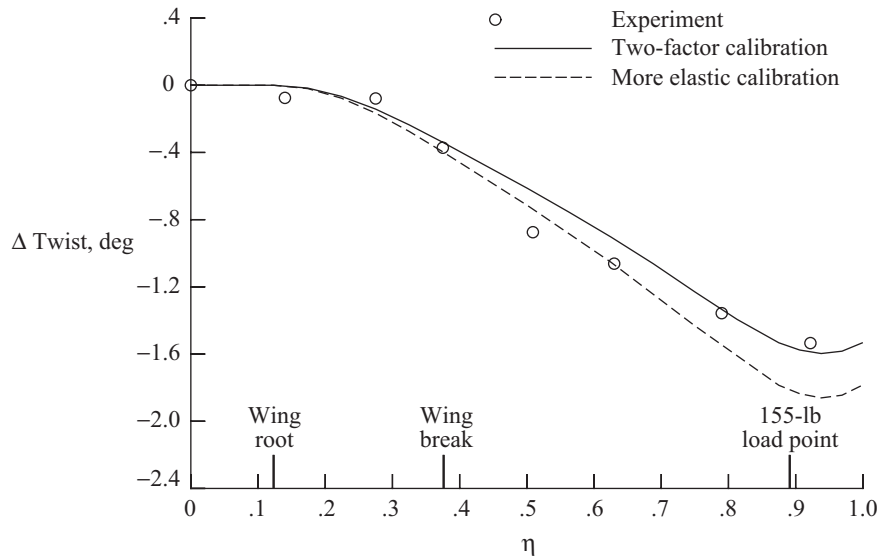


Figure 20. Static-load wing-twist increment for recalibration of input to the ELAPS code.

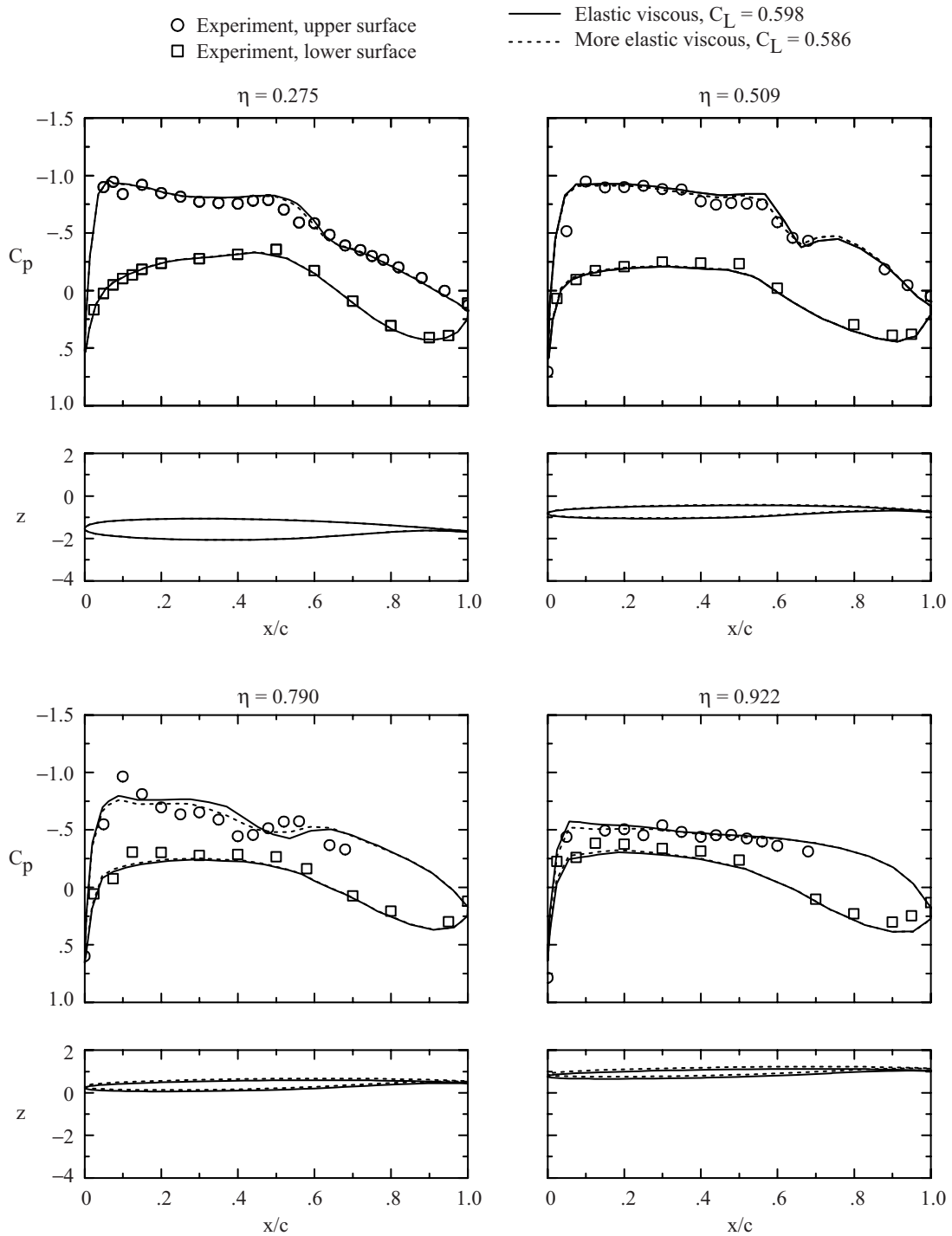


Figure 21. Effect of more elastic calibration on wing pressure distributions and deformations for wind-tunnel case 3:  $M_\infty = 0.819$ ;  $\alpha = 1.98^\circ$ ;  $R_{\bar{c}} = 13 \times 10^6$ ;  $q_\infty = 1736$  psf;  $C_L = 0.541$ .

REPORT DOCUMENTATION PAGE				Form Approved OMB No. 0704-0188	
<p>The public reporting burden for this collection of information is estimated to average 1 hour per response, including the time for reviewing instructions, searching existing data sources, gathering and maintaining the data needed, and completing and reviewing the collection of information. Send comments regarding this burden estimate or any other aspect of this collection of information, including suggestions for reducing this burden, to Department of Defense, Washington Headquarters Services, Directorate for Information Operations and Reports (0704-0188), 1215 Jefferson Davis Highway, Suite 1204, Arlington, VA 22202-4302. Respondents should be aware that notwithstanding any other provision of law, no person shall be subject to any penalty for failing to comply with a collection of information if it does not display a currently valid OMB control number.</p> <p><b>PLEASE DO NOT RETURN YOUR FORM TO THE ABOVE ADDRESS.</b></p>					
1. REPORT DATE (DD-MM-YYYY)		2. REPORT TYPE		3. DATES COVERED (From - To)	
01- 03 - 2003		Technical Publication			
4. TITLE AND SUBTITLE Static Aeroelastic Predictions for a Transonic Transport Model Using an Unstructured-Grid Flow Solver Coupled With a Structural Plate Technique				5a. CONTRACT NUMBER	
				5b. GRANT NUMBER	
				5c. PROGRAM ELEMENT NUMBER	
6. AUTHOR(S) Allison, Dennis O.; and Cavallo, Peter A.				5d. PROJECT NUMBER	
				5e. TASK NUMBER	
				5f. WORK UNIT NUMBER 719-10-40-10	
7. PERFORMING ORGANIZATION NAME(S) AND ADDRESS(ES) NASA Langley Research Center Hampton, VA 23681-2199				8. PERFORMING ORGANIZATION REPORT NUMBER  L-18027	
9. SPONSORING/MONITORING AGENCY NAME(S) AND ADDRESS(ES) National Aeronautics and Space Administration Washington, DC 20546-0001				10. SPONSOR/MONITOR'S ACRONYM(S)  NASA	
				11. SPONSOR/MONITOR'S REPORT NUMBER(S) NASA/TP-2003-212156	
12. DISTRIBUTION/AVAILABILITY STATEMENT Unclassified - Unlimited Subject Category 02 Availability: NASA CASI (301) 621-0390      Distribution: Standard					
13. SUPPLEMENTARY NOTES Allison, NASA Langley Research Center. Cavallo, Presently at Combustion Research and Flow Technology, Inc., Dublin, PA. An electronic version can be found at <a href="http://techreports.larc.nasa.gov/ltrs/">http://techreports.larc.nasa.gov/ltrs/</a> or <a href="http://techreports.larc.nasa.gov/cgi-bin/NTRS">http://techreports.larc.nasa.gov/cgi-bin/NTRS</a>					
14. ABSTRACT An equivalent-plate structural deformation technique was coupled with a steady-state unstructured-grid three-dimensional Euler flow solver and a two-dimensional strip interactive boundary-layer technique. The objective of the research was to assess the extent to which a simple accounting for static model deformations could improve correlations with measured wing pressure distributions and lift coefficients at transonic speeds. Results were computed and compared to test data for a wing-fuselage model of a generic low-wing transonic transport at a transonic cruise condition over a range of Reynolds numbers and dynamic pressures. The deformations significantly improved correlations with measured wing pressure distributions and lift coefficients. This method provided a means of quantifying the role of dynamic pressure in wind-tunnel studies of Reynolds number effects for transonic transport models.					
15. SUBJECT TERMS Static aeroelastic predictions; Structural plate technique; Reynolds number effects; Unstructured grid; Transonic flow; Interactive boundary layer; Wind-tunnel model					
16. SECURITY CLASSIFICATION OF:			17. LIMITATION OF ABSTRACT	18. NUMBER OF PAGES	19a. NAME OF RESPONSIBLE PERSON
a. REPORT	b. ABSTRACT	c. THIS PAGE			STI Help Desk (email: <a href="mailto:help@sti.nasa.gov">help@sti.nasa.gov</a> )
U	U	U	UU	51	19b. TELEPHONE NUMBER (Include area code) (301) 621-0390